Surface & Coatings Technology 480 (2024) 130613

Contents lists available at ScienceDirect

Surface & Coatings Technology

journal homepage: www.elsevier.com/locate/surfcoat

Pulsed electrodeposition of homogenous and heterogeneous solid solution layered structure in high strength nanocrystalline Co—Cu alloys

Killang Pratama [a,*], Chunhua Tian [a], Amit Sharma [a], Maria Watroba [a], Jenő Gubicza [b], Bonita Dilasari [c], Jakob Schwiedrzik [a,1], Johann Michler [a,1]

[a] EMPA - Swiss Federal Laboratories for Materials Science and Technology, Laboratory for Mechanics of Materials and Nanostructures, CH-3602 Thun, Switzerland
[b] Eötvös Lorand University, Department of Materials Physics, H-1518 Budapest, Hungary
[c] Institute Technology of Bandung, Department of Metallurgical Engineering, ID-40132 Bandung, Indonesia

ARTICLE INFO

Keywords:
Nanocrystalline alloys
Solid solution structure
Pulsed deposition
micro-mechanics

ABSTRACT

A supersaturated solid solution nanostructure of an immiscible Co—Cu system is among the promising nanocrystalline (NC) alloys offering enhanced thermal and mechanical stability. In this paper, experiments were conducted to study the phase transformation and tailoring microstructure from a homogeneous/single-phase to a heterogeneous/dual-phase solid solution layered Co—Cu nanostructure via pulsed electrochemical deposition (PED). The increasing concentration of sodium dodecyl sulfate (SDS) in electrolyte played a crucial role in stabilizing a homogeneous solid solution Co—Cu nanostructure. On the other hand, the opposite approach led to the formation of heterogeneous solid solution Co—Cu alloys in the form of multilayered nanostructure consisting of the primary and secondary solid solution Co—Cu differing in 10–15 at.% Cu. The separation of primary and secondary phase is more prominent with the extended pulsed periods. The mechanical properties of selected single- and dual-phase alloys were investigated through micro-pillar compression, revealing that a combination of a high yield strength and an elevated strain hardening can be achieved in NC materials through a combined solid solution strengthening and hardening through nano-twin (NT).

1. Introduction

Nanocrystalline (NC) Co—Cu alloys [1–5] are receiving great interest for their significant improvement in thermal and mechanical stability compared to their NC pure metals counterparts [6–11]. Electrochemical deposition is among favored techniques for producing bulk nanostructured materials due to a low energy consumption, a simple route of production, and a tunable material properties. The application of pulsed-current allows even a wider range of control for compositional and microstructural modification of electrodeposited NC Co—Cu alloys. Prior to this study, electrodeposition of NC Co—Cu alloys have been developed using direct-current (DC) or pulsed-current (PC), producing different types of microstructures including a supersaturated solid solution [4,5,12], an immiscible phase structure [13–16], and a nanoscale lamellar microstructure [17–19]. Pulsed electrochemical deposition (PED) of NC Co—Cu alloys can be also performed for producing a wide range of chemical composition (5–50 at.% Cu), which results in diverse microstructures. For instance, the higher Cu content has a tendency to the formation of larger size of grains in PED-processed Co-rich NC Co—Cu with a solid solution structure [20].

From a mechanical standpoint, a bulk sample of electrodeposited immiscible Co—Cu alloy (7 wt% Cu) with a high density of fine nanoscale lamellar structures showed the highest yield strength (1.42 GPa) among the Co—Cu alloys reported in the literature [17]. This lamellar structure provided also an improved saturation magnetization compared to NC Co [18]. However, it exhibited the lowest ductility in this group of materials with a strain to failure of below 5%. A significant improvement in ductility has been observed for a bulk PED-processed NC Co—Cu (28 at.% Cu) with a strain to failure as high as 16% with the apparent strain hardening [5]. Moreover, the yield strength (1.21 GPa) for this alloy remained high compared with the lamellar structure. An enhanced mechanical performance in this alloy could be influenced by some factors such as the different Co—Cu composition, the solid solution strengthening, and the implementation of pulsed current. Great interest is also received by an immiscible and a multi-layered structure of NC Co—Cu alloys for their unique giant magnetoresistance (GMR)

* Corresponding authors.
E-mail address: killang.pratama@empa.ch (K. Pratama).
[1] Shared senior authorship.

https://doi.org/10.1016/j.surfcoat.2024.130613
Received 29 December 2023; Received in revised form 22 February 2024; Accepted 29 February 2024
Available online 5 March 2024

effect originating from the modulated nanostructures of Co and Cu [21,22]. However, information about the mechanical properties of these two-phase nanostructured alloys is so far very limited [19].

The chemical composition and microstructure of electrodeposited NC Co—Cu alloys were governed by the selection of PED parameters and organic additives [14,15,20]. Sodium dodecyl sulfate (SDS) is among the organic additives and surfactant extensively used in industrial electroplating as a wetting agent. This anionic surfactant functionally plays a crucial role on reducing surface tension and detachment of hydrogen bubbles from the cathode surface during deposition [23,24]. At the same time, adding SDS into the electrolyte in appropriate concentration also reduces surface roughness and grain size (GS) of the electroplated metals and alloys [25,26]. This is especially beneficial for applications where superior surface quality and mechanical strength are essential, such as fabrication of micro-architecture components through the template assisted electrochemical deposition (TAED) process [27–30]. The mentioned benefits are originated from the adsorption of this surfactant on the electrode surface, which changes its surface characteristic. Consequently, the surfactant can limit the approach of selected ionic compounds within the electrical double layer (EDL) and reduce the active sites for heterogeneous nucleation [31,32]. However, the role of SDS in PED of Co—Cu remains unclear whether this anionic surfactant create a preferred bonding with Co or Cu cations, resulting in Co—Cu films with the different chemical composition [14,20]. This is especially relevant in the presence of another organic additive, acting also as a grain refiner (e.g., saccharin). Interestingly, it was observed that NC Co—Cu films deposited with a combined SDS and saccharin exhibited a face-centered cubic (fcc) structure with a strong intensity of (111) peak [14,20]. Comprehensive understand of this mechanism will lead to a better approach in designing Co—Cu composition using this organic additive.

This work is aimed at exploring the relationship between the PED-processing parameters with the chemical composition, microstructure, and mechanical properties of NC Co—Cu. We investigated the formation of a homogeneous and a heterogeneous solid solution layered structures in PED-processed NC Co—Cu alloys through variation in the concentration of SDS in the electrolyte and the pulse period of the deposition process. The chemical composition and microstructure were investigated by scanning electron microscope (SEM), energy dispersive X-ray spectroscopy (EDS), X-ray diffraction (XRD), and transmission electron microscope (TEM). The mechanical properties of selected samples were investigated using in-situ micro-pillar compression experiments. The identified process-structure-property relationships act as a baseline to optimize the electrolyte composition and deposition process for a given target application such as TAED of complex micro-component or metamaterials.

2. Materials and experimental methods

2.1. Electrochemical analysis and deposition

Electrochemical analysis and deposition were carried out by using Metrohm Autolab PGSTATs (Metrohm AG, Herisau, Switzerland) in the Co(II)-tartrate complex containing solution. The solution is adapted from the research studied electrodeposition of NC Co [33] and Co—Cu alloys [4,5,12,22], comprising 0.40 M $CoSO_4.7H_2O$, 0.04 M $CuSO_4.5H_2O$, 1.00 M Na_2SO_4, 0.30 M H_3BO_3, and 0.20 M $KNaC_4H_4O_6.4H_2O$ as a tartrate complex former. The organic additives used in this study are 2.00 g/L $C_7H_5NO_3S$ (saccharin) and 0.30–1.50 g/L $C_{12}H_{25}NaO_4S$ (SDS). A conductive Au-wafer and a Pt-coated titanium mesh were used as working electrode (WE) and counter electrode (CE), respectively. The relative potential of the WE was measured against the Ag/AgCl reference electrode (RE). Prior to the electrochemical testing and deposition, the WE surface was subjected to ultrasonic cleaning with acetone, isopropanol, and deionized (DI) water. Electrochemical tests and deposition were performed in a 250 mL jacketed glass beaker integrated with a water thermostat for maintaining deposition temperature at 40 °C. Linear sweep voltammetry (LSV) potentiostatic measurements were carried out from 0 V to −1.3 V vs. Ag/AgCl with a scan rate at 0.1667 mV/s [34] on the WE with a free surface diameter of 5 mm. PED of 15–20 μm thick films of NC Co—Cu alloys was performed on 1 cm^2 area of the WE surface in pulsed galvanostatic or chronopotentiometry mode with a fixed pulsed current density of 1000 A/m^2. The on-time pulse length was varied at 2 ms, 5 ms, and 50 ms with a constant 10% of duty-cycle. Direct current (DC) electrodeposition was also performed at a constant current density of 100 A/m^2.

2.2. Material characterization

Surface characterization of Co—Cu deposits was performed in SEM (TESCAN MIRA, Brno, Czech Republic) equipped with an EDS detector (EDAX, AMETEK Inc., Pleasanton, USA) for compositional analysis. EDS analysis were conducted out on polished cross-sections of deposits to gather the depth of thickness chemical composition. XRD (Bruker D8 Discovery X-ray Diffractometer, Billerica, USA) measurements were carried out in Bragg-Brentano configuration using a $CuK\alpha_1$ radiation source ($\lambda = 1.5406$ Å). Peak profile analysis of the XRD patterns were performed in the Fityk software (Institute of high pressure physics, Warsaw, Poland) [35] with a Pseudo-Voigt fit function. The crystallite size determination was carried out through the Williamson-Hall (W—H) method to distinct the crystallite size and the micro-strain effect on the peak profile breadth [36]. The integral breadth of the XRD peaks was analyzed in the W—H plots. TEM investigations were performed on the cross-section TEM lamella prepared by focused ion beam/FIB milling (TESCAN LYRA3, Brno, Czech Republic). TEM Bright field imaging was carried out using a Themis 200 G3 aberration (probe) corrected TEM (Thermo Fischer Scientific, Waltham, USA) operating at 200 kV. The elemental area maps were acquired using EDS in scanning-transmission (STEM) mode. The orientation and size distribution of the grains was measured with the scanning precession electron diffraction (SPED) technique in the TEM-based orientation imaging microscopic (OIM) analysis using NanoMegas A-STAR (NanoMEGAS SPRL, Brussel, Belgium) [37]. A step size of 3 nm and a precession of 0.6° was used for all measurements. The raw data sets of the SPED based orientation maps were processed and analyzed with the TSL OIM Data Analysis software (EDAX, AMETEK Inc., Pleasanton, USA). Grain was defined as a set of at least 5 pixels with a misorientation angle between neighboring grains higher than 15°.

2.3. Micropillar fabrication and compression

Micropillar compression tests were conducted to compare the mechanical properties of the selected homogeneous and heterogeneous solid solution NC Co—Cu samples. The micropillars were fabricated by FIB (TESCAN LYRA3, Brno, Czech Republic) milling with the Ga^+ ion source under 30 kV acceleration voltage, starting from a rough cut using 5 nA, to finer milling by 1 nA and brought into final shape using 200 pA polishing. Micropillars have a diameter of approximately 5 μm with an aspect ratio of 2 (height/diameter). Pillar compression was performed in a Philipps XL30 SEM (Eindhoven, Netherlands), equipped with an Alemnis indenter system (Alemnis AG, Thun, Switzerland). A flat punch of diameter 10 μm was used and all test were performed at an applied quasistatic strain rate of 10^{-3} s^{-1}.

3. Results and discussion

3.1. Electrochemical analysis and alloy composition

LSV analysis was carried out to investigate the electrochemical behavior of the Co—Cu electrolyte containing different concentrations of SDS. The theoretical deposition rate and the possible chemical processes during deposition can be predicted from this analysis. The

measured LSV curves (Fig. 1a) show a broader range of current density for the deposition of Co at the higher concentration of SDS. The starting deposition potential for Co is also shifted to the more positive values indicating a more favorable condition for the deposition of Co. On the other hand, the maximum deposition rate of Cu is constrained by this element's limiting current density in the range of 20–30 A/m^2 and rather constant at the varied concentrations of SDS tested here. To validate the influence of SDS concentration on the chemical composition of Co—Cu deposit, DC electrodeposition was carried out at a lower current density (100 A/m^2) than applied for PED-process (1000 A/m^2) to prevent the hydrogen evolution reaction as predicted from LSV analysis. Fig. 1b shows the potential profiles during DC deposition showing the shifts of deposition potential to a more positive value at a higher SDS concentration, which is in good agreement with LSV analysis. EDS compositional analysis confirms a significant increase in Co concentration from 63.2 ± 1.4 at.% to 72.6 ± 1.3 at.% with an increasing concentration of SDS from 0.3 g/L to 1.0 g/L as shown in Table 1. LSV and DC deposition analysis validates a significant influence of SDS concentration in promoting the deposition of Co over Cu, which leads to incorporation of more Co in the Co—Cu deposit.

PED of Co—Cu alloys was carried out at different pulse lengths and SDS concentrations. The representative profiles of potential and current density during PED process were also recorded as shown in Fig. 2 for different pulsed lengths and Fig. 3 for varied SDS concentrations. Firstly, the influence of the pulse length on the PED process of Co—Cu was studied at a constant 1.0 g/L SDS. The representative current density profiles for this analysis are presented in Fig. 2a-c showing a strong capacitance effect for 2 ms on-time process. This effect is attributed to the EDL charge-discharge mechanisms and the adsorption-desorption of ions and additives during the on- and off-time [15,38]. The capacitance effect gradually drops with extending pulsed length to 5 ms and 50 ms on-time processes. The corresponding potential profiles during PED process for this analysis are presented in Fig. 2d,e showing the shift of the on-time potential to more negative values with extending pulse length. In this particular case, more negative values is suggested due to the higher potential drop across the thicker pulsating Nernst diffusion layer (δ_p) built up during PED process, which is proportional to the square root of the pulse on-time length (t_{on}), $\delta_p = \sqrt{2Dt_{on}/\pi}$, as described by Ibl [38]. The parameter D is the diffusion coefficient of ions. Here, the off-time potential also needs to increase to more positive values for the longer pulse lengths to compensate the relaxation/recovery stage of the thicker diffusion layer during the off-time. This is also validated by the pronounced shifts of the off-time potentials to more positive values as shown in Fig. 2d,e. Overall, for a single pulse cycle, the potential profile analysis shows the broader range of potential (ΔE) with the extended pulse lengths. Pulse galvanostatic analysis shows the significant influences of the pulse length on the EDL charge-discharge mechanisms and the possible thickness of the diffusion layer, which may have the influence on the PED of Co—Cu process, resulting in diverse chemical compositions and microstructures.

Fig. 3 shows the potential profiles during PED of Co—Cu at varied concentration of SDS with a constant pulse length of 5 ms on-time and 45 ms off-time. The profiles show a minor shift of the on-time potential to more positive values with increasing concentration of SDS, which is in good agreement with the LSV and DC deposition analysis. The increasing concentration of SDS also leads to a minor shift of the off-time potential to more negative values. Overall, the potential range (ΔE) for pulsed deposition is slightly reduced with the increasing concentration of SDS.

Table 1
EDS compositional analysis from the cross-section of NC Co—Cu deposited at varied deposition parameters and SDS concentrations. i_p: pulsed current density; t_{on}: pulse-on time; t_{off}: pulse-off time.

Name of samples	PED-processing parameters			SDS (g/L)	Composition of deposit	
	i_p (A/m^2)	t_{on} (ms)	t_{off} (ms)		Co (at. %)	Cu (at. %)
S1	100	Direct current (DC)		0.3	63.2 ± 1.4	36.8 ± 2.5
S2				0.5	70.7 ± 1.3	29.3 ± 2.7
S3				1.0	72.6 ± 1.3	27.4 ± 2.7
S4	1000	2	18	0.3	69.8 ± 1.7	30.2 ± 2.7
S5				0.5	69.5 ± 1.7	30.5 ± 2.7
S6				1.0	69.8 ± 1.7	30.2 ± 2.8
S7	1000	5	45	0.3	64.4 ± 1.4	35.6 ± 2.6
S8				0.5	68.3 ± 1.3	31.7 ± 2.7
S9				1.0	71.6 ± 1.3	28.4 ± 2.8
S10				1.5	76.0 ± 1.3	24.0 ± 2.8
S11	1000	50	450	1.0	63.9 ± 1.4	36.1 ± 2.6

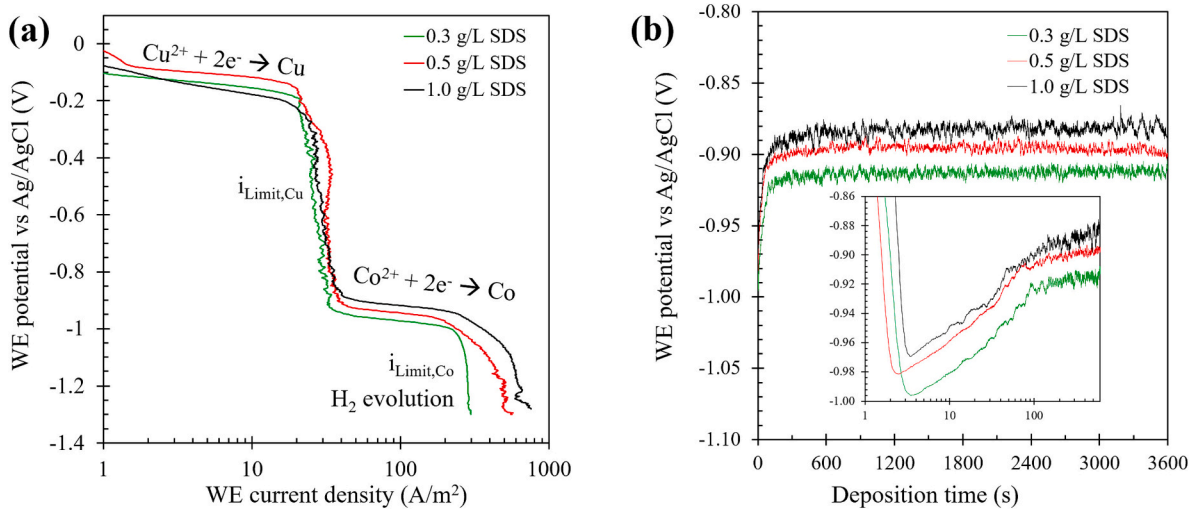

Fig. 1. (a) The LSV potentiostatic curves for the electrolytes with different concentrations of SDS (scan rate: 0.1667 mV/s). (b) The potential profiles recorded during DC electrodeposition (100 A/m^2) of Co—Cu with different concentration of SDS.

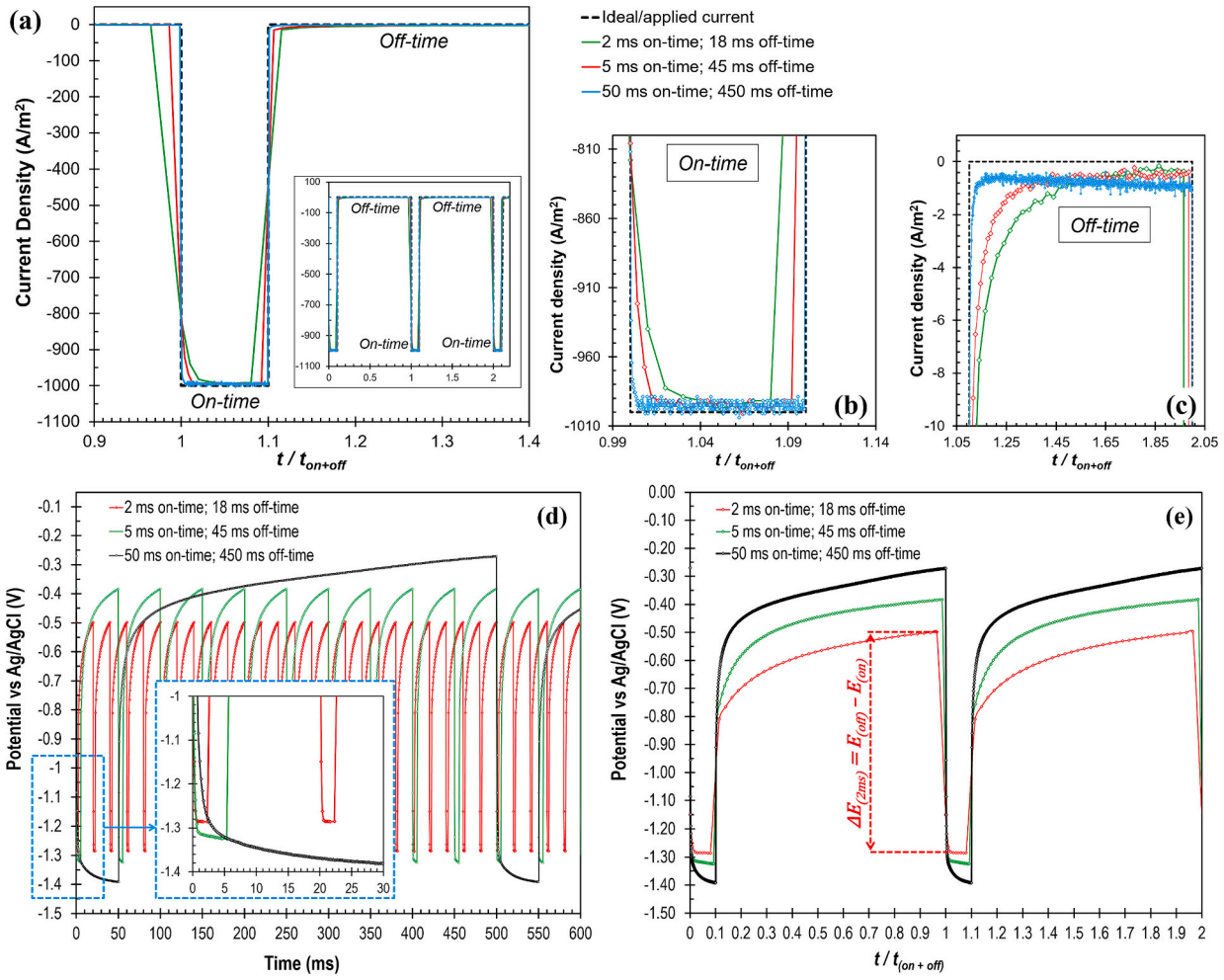

Fig. 2. The profiles of (a-c) current density and (d-e) potential recorded during PED of Co—Cu at varied length of pulsed (10% of duty cycle) with a constant 1.0 g/L SDS. The sampling time interval (Δt) was configured at 200 μs for all measurements.

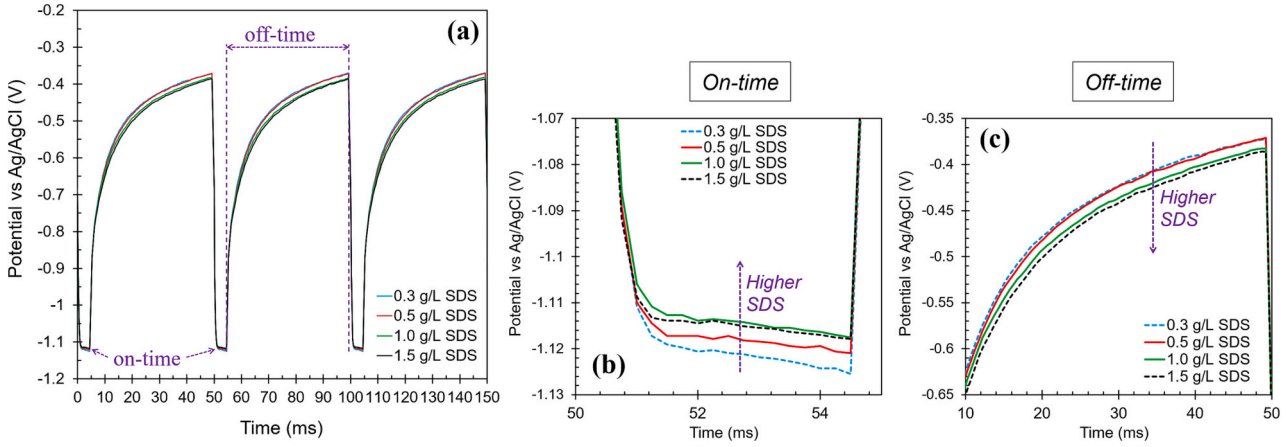

Fig. 3. The potential profiles recorded during PED of Co—Cu at varied SDS concentration (0.3–1.5 g/L) with a constant pulsed length of 5 ms on-time and 45 ms off-time. The sampling time interval (Δt) was configured at 200 μs for all measurements.

The concentration of SDS shows only a minor influence on the PED processes of Co—Cu that can be investigated using this analysis. To sum up, LSV and DC deposition analysis showed a significant influence of SDS concentration to promote the deposition of Co under continuous and constant current, but this effect is only slightly observable under pulsed current performed using pulse galvanostatic analysis.

EDS measurements were performed to confirm the influence of the pulse lengths and SDS concentrations on the chemical composition deposition Co—Cu alloys and the results are presented in Table 1. The first series of samples deposited at 2 ms on-time (S4 - S6) showing a rather constant Co and Cu composition at the varying SDS concentration. On the other hand, the increasing concentration of SDS leads to the

size reduction of the globular structure on the planar view of surface films (Fig. 4a-c). The globular structure is among the types of a combined 2D field-oriented texture (FT) and 3D un-oriented dispersion (UD) type crystal growth deposit, which is developed during the electrochemical nucleation and growth of crystals at the high current density and inhibition intensity [39]. For the extended pulse length of 5 ms on-time and 45 ms off-time (S7 – S10), the increasing concentration of SDS yields a significant Co enrichment in the chemical composition and the finer globular structure (Fig. 4d-g). The sample deposited at 1.5 g/L SDS shows even the nanometer-sized globular structure resulting in the finest surface morphology (Fig. 4g). PED of Co—Cu alloys was also carried out for a long on-time of 50 ms, showing the lowest concentration of Co (63.9 ± 1.4 at.%). This sample also shows a slight change of the typical surface morphology observed from other samples (Fig. 4h). In summary, electrochemical and chemical composition analysis confirms a significant impact of the pulse length and SDS concentration on the chemical composition of PED-processed Co—Cu alloys, which results in diverse surface quality of deposits.

3.2. XRD line profile analysis

Microstructure characterization of PED-processed Co—Cu alloys was performed through XRD line profile analysis. XRD investigations show a significant influence of the SDS concentration and the pulse length on the formation of diverse microstructures and phases in the Co—Cu system (see Fig. 5a). For all samples, fcc reflections with the indices (111), (200), (220), (311), and (222) were detected in the XRD spectra. Each refection consisted of two close peaks. In the left part of Fig. 5a, the parts of the XRD patterns related to the 2θ diffraction angle values between 42° and 52° are shown. Due to the crystallographic texture of the layers, the (111) peaks are very strong, and the other reflections are weak for all deposition conditions. Therefore, the parts of the XRD patterns related to 2θ angles higher than 45° are presented with a magnified intensity at the right part of Fig. 5a.

Fig. 5b shows the XRD patterns for a group of samples deposited at 2 ms on-time at 2θ angles between 42° and 45°. For each XRD pattern, a shoulder is detected at the left side of the main Co—Cu (111) peak, which may be attributed to a secondary phase. The lower angle of the secondary phase peak suggests a higher lattice constant compared to the main Co—Cu phase. The peak position of the main phase is between the reference locations of the reflections for pure fcc Cu and fcc Co (see Fig. 5b), suggesting that the main phase is a fcc Co—Cu solid solution. The higher lattice constant for the secondary phase can be caused by a higher Cu content. The peak intensity of this secondary phase decreases gradually with the increasing concentration of SDS from 0.3 g/L to 1.0 g/L as shown in Fig. 5b. The reduction of the fraction of the secondary phase should yield an increase of the concentration of Cu atoms in the primary Co—Cu phase. Indeed, this effect is indicated by the shift of the (111) peak position of the main Co—Cu phase closer to the reference peak position of Cu (111). Based on EDS elemental analysis (Table 1), it was found that this group of samples exhibits an identical Co—Cu composition with ~31 at.% Cu. Therefore, the changes in the XRD spectra are not caused by changes in chemical composition. The higher SDS concentration may contribute to the formation and stabilization of a homogenous solid solution Co—Cu nanostructure.

The XRD patterns of a group of samples deposited at 5 ms on-time show an even more distinct phase transition from a homogeneous to a heterogeneous structure as SDS concentration decreases from 1.5 g/L to 0.3 g/L (see Fig. 5a). For the highest concentration of SDS (1.5 g/L), a single peak was detected for each fcc XRD reflection, suggesting a single/homogeneous Co—Cu solid solution structure. The phase separation was started with the decreasing concentration of SDS to 1.0 g/L, where a double (111) peak is detected. The right part of the (111) peak is attributed to the primary Co—Cu phase with a lower Cu concentration than the secondary fcc phase related to the left component of the (111) peak. The close positions of the two adjacent (111) peaks suggests that the Cu content is almost identical in these two solid solution Co—Cu structures differing for approximately 3.98–4.71 at.% Cu estimated from our analysis (see Supplementary Materials A). A more pronounced phase separation is visible with a further decrease in SDS concentration to 0.5 g/L. In these samples, the double peaks are detected not only for (111) reflection, but also for (311) and (222) peaks. The peak intensity of the secondary phase also intensifies with the decreasing concentration of SDS to 0.3 g/L. For the extended pulse period of 50 ms on-time, XRD analysis shows an enhanced peak intensity of the Cu-richer fcc phase (see Fig. 5a), suggesting an elevated fraction of this secondary phase.

The crystallite size of the NC Co—Cu deposits was determined from the XRD peak breadth using the Williamson-Hall (WH) analysis [40] as described by the following equation.

$$\left(L\cos\theta_{peak}\right) = \varepsilon\left(4\sin\theta_{peak}\right) + \frac{K\lambda}{D} \quad (1)$$

The integral breadth (L) of the individual peaks (θ_{peak}) was obtained

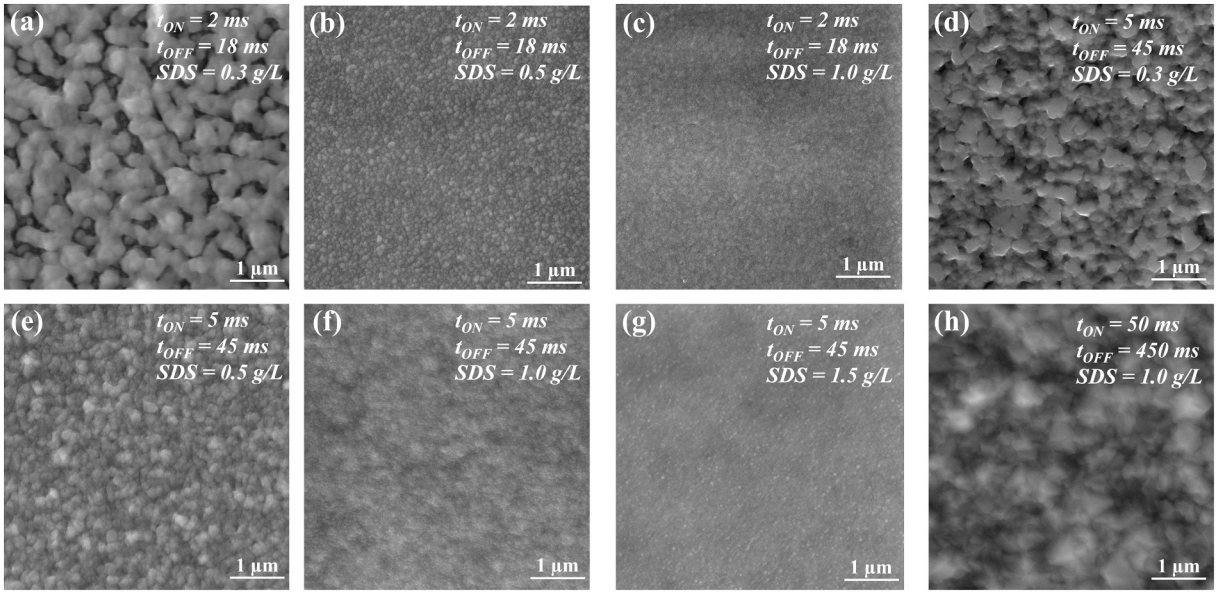

Fig. 4. SEM micrographs showing the surface morphology of 15–20 µm thick films of Co—Cu alloys deposited with varying SDS concentrations and pulse periods.

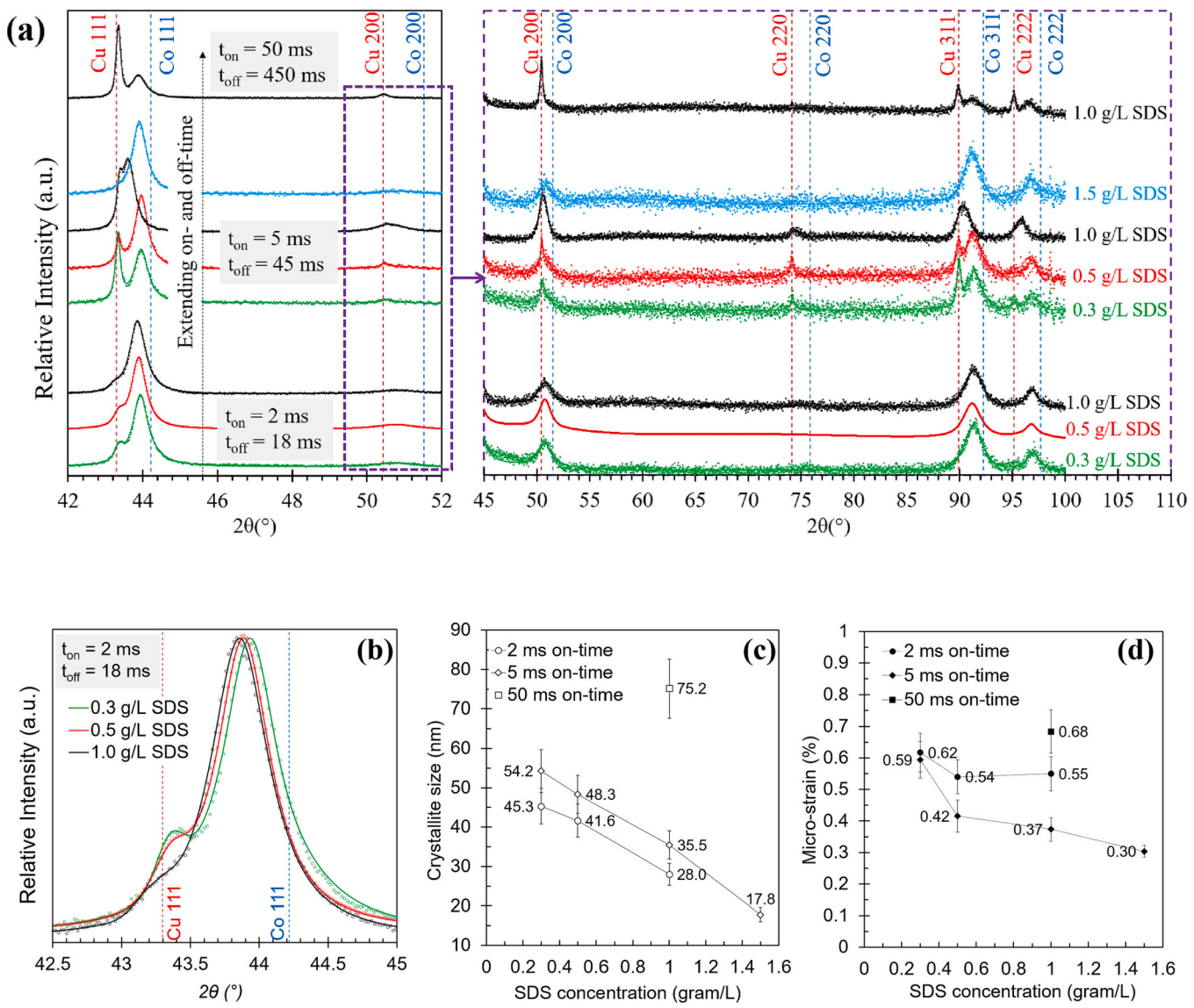

Fig. 5. (a) XRD patterns of Co—Cu alloys deposited at varied pulsed period and concentration of SDS. The reference diffraction peak position of Cu (No. 4–836) and Co (No. 15–806) from JCPDS-ICDD ©1994 files are presented with the vertical red and the blue dashed lines, respectively. (b) Detailed XRD reflection (111) for the samples deposited at 2 ms on-time. (c) The crystallite size and (d) micro-strain profiles of Co—Cu deposits as a function of SDS concentration estimated from Williamson-Hall plots of harmonic pair of (111)–(222) XRD reflections.

by fitting the two overlapping reflections in each fcc peak using two pseudo-Voigt functions. For samples exhibiting double fcc peaks, the crystallite size analysis (D) was performed only for the fcc peaks at the higher diffraction angles since these reflections are related to the primary Co—Cu phase, which is the main phase for most deposited samples. The rest parameters from Eq. (1) correspond to the lattice micro-strain (ε), the dimensionless shape factor (K = 0.9), and X-ray wavelength (λ: 0.15406 nm). In the present work, the crystallite size determination was carried out by evaluating the harmonic reflection pair of (111)–(222). This method has been used successfully by Bakonyi et al. for studying fcc-structured polycrystalline Co [41]. The Williamson-Hall plots for the crystallite size determination is available in Supplementary Materials B.

Fig. 5c shows the crystallite size profiles as a function of SDS concentration for samples deposited at varied pulse lengths, while the corresponding lattice micro-strain (ε) profiles are depicted in Fig. 5d. For NC materials, the crystallite size is frequently comparable with the grain size of materials. The crystallite/grain size profiles confirm that SDS plays a crucial role for grain size reduction in PED-processed NC Co—Cu. For a series of sample deposited at 5 ms on-time, the grain size decreases with a factor of three from ~54 nm to ~18 nm with increasing SDS concentration from 0.3 g/L to 1.5 g/L. In addition, the grain size also reduces with the decreasing pulse length. Fig. 5c shows that among the studied samples the single-phase Co—Cu alloys deposited at 5 ms on-time with 1.5 g/L SDS exhibits the smallest grain size (~18 nm).

The micro-strain profiles (Fig. 5d) observe that the lattice micro-strain tends to increase with the decreasing concentration of SDS. For low concentration of SDS (≤ 1.0 g/L), the formation of dual-phase structure is established and the fraction of secondary phase grows with the decreasing concentration of SDS (see Fig. 5a). Thus, the rising trend of lattice micro-strain may be attributed by the increasing number of dislocations generated to reduce the mismatch stress at the interface between the primary and secondary phases. This particular dislocation is not visible in a single-phase alloy deposited with 1.5 g/L SDS and 5 ms on-time due to absence of secondary phase and generated mismatch stress, resulting in the smallest lattice micro-strain calculated here (see Fig. 5a).

3.3. TEM analysis

TEM/STEM analysis were carried out to investigate the microstructure and elemental distribution analysis for the homogeneous and heterogeneous phase of NC Co—Cu alloys deposited with different concentration of SDS as observed from XRD line profile analysis. Here, two samples exhibited a homogeneous (sample *S10*) and a heterogeneous (sample *S8*) phases were selected for this analysis, which were deposited at the same pulse period of 5 ms on-time differing in SDS concentrations at 1.5 g/L *(S10)* and 0.5 g/L *(S8)* as defined in Table 1. TEM analysis was performed to obtain the high magnification microstructure image, while STEM-EDS and TEM-OIM techniques were carried out for elemental distribution and grain orientation analysis, respectively. All measurements were carried out on TEM-lamella samples taken for few microns depth of thickness from the top surface of selected deposits.

3.3.1. Homogeneous/single-phase NC Co—Cu alloy

Fig. 6a depicts a TEM bright field (BF) image of the cross-sectional microstructure of a sample *S10* deposited with 1.5 g/L SDS, showing the nanostructured grains in the Co—Cu film regime. Several nano-twins were also detected from this analysis, as marked with the yellow arrows in Fig. 6b. In addition, a number of columnar grains packed with a high density of horizontally-oriented NTs is also observable as depicted in Fig. 6c. The corresponding selected area electron diffraction (SAED) pattern (Fig. 6d) for this sample detects only single face-centered cubic (fcc) peaks, conforming to the corresponding XRD spectra of this sample as shown in Fig. 5a. STEM-EDS analysis (Fig. 6e-g) for this alloy shows a fairly uniform elemental distribution of Co and Cu, validating a homogeneous solid solution Co—Cu nanostructure or so called as a single-phase alloy. Apparently, some spots with imperfect homogeneous composition of Co and Cu are observed from the EDS maps, but neither elemental segregation nor regular strong compositional fluctuation is detected from this analysis.

Fig. 7a shows an inverse pole figure (IPF) map of cross-sectional microstructure analysis of a homogeneous/single-phase alloy performed using TEM-based OIM. A single-phase alloy (Fig. 7b) contains a uniform distribution of nanostructured grains from 5 nm to 120 nm with a mean grain size of 40 ± 2.5 nm. It must be noted that the grain size from XRD peak breadth differs with TEM-OIM analysis (~40 nm) due to the different measurement and analysis techniques, which is further discussed in Section 3.3.4. IPF texture analysis shows that the nanostructured grains tend to growth in the predominantly {111} texture along the growth direction as depicted in Fig. 7c. A number of large columnar grains with sizes of 100–200 nm are also detected here. Misorientation angle analysis confirms that the columnar grains consist of horizontally oriented NT structures, which are validated with the 60° misorientation angles performed within the selected grains as presented in Fig. 7d,e. This could be the typical horizontally oriented NT structures observed from TEM-BF analysis as depicted in Fig. 6c. The columnar

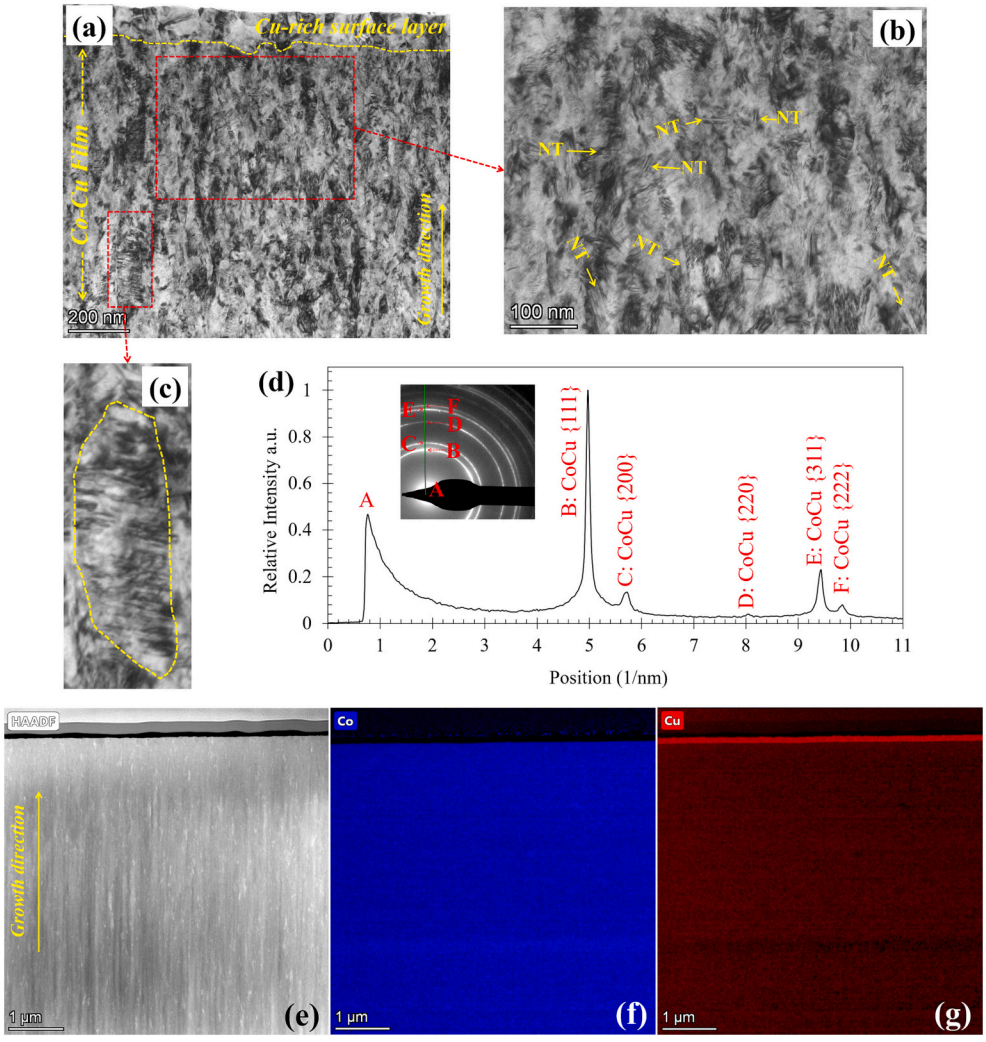

Fig. 6. TEM and STEM-EDS analysis from the cross-section of a homogenous/single-phase Co—Cu alloy deposited with 1.5 g/L SDS (sample *S10*): (a-c) TEM-BF images and (d) corresponding SAED pattern in Co—Cu film regime. (e) High angle angular dark-filed (HAADF) and EDS map of (f) Cu and (g) Co.

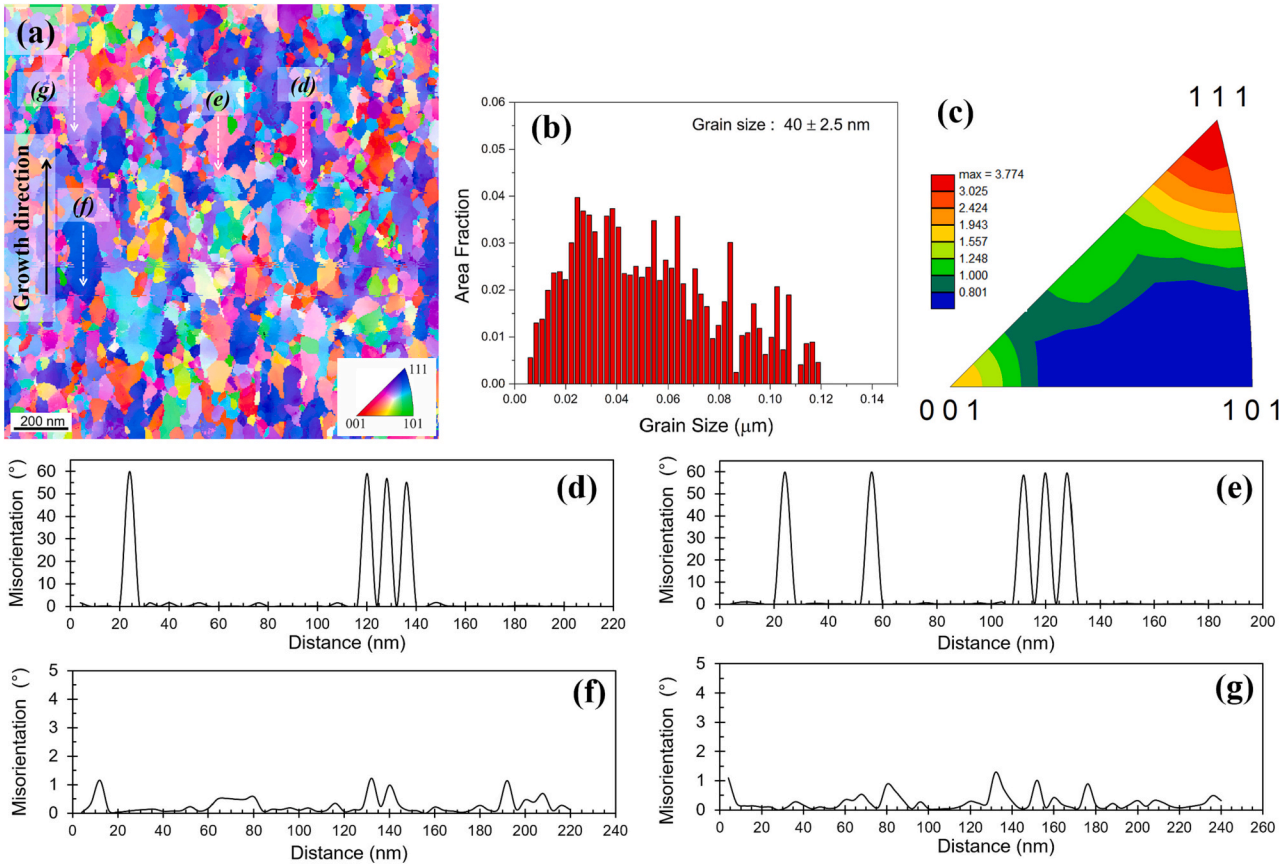

Fig. 7. TEM-OIM microstructure analysis from the cross-section of homogeneous/single-phase Co—Cu alloys: (a) Inverse pole figure (IPF) map with the corresponding (b) grain size distribution and (b) IPF texture analysis. (d-g) Misorientation angle profiles evaluated for the large columnar grain as marked with the white arrows in (a).

grains can be also attributed to sub-grains with low misorientation angles of below 2° as depicted in Fig. 7f,g.

3.3.2. *Heterogeneous/dual-phase NC Co—Cu alloy*

TEM-BF images of a sample *S8* deposited with 0.5 g/L SDS also displays a NC structure in a major part of Co—Cu film (Fig. 8a) with several NTs as marked with the red arrows in Fig. 8b. In contrast to the single-phase alloy, the strong intensity of a double {111} peak (B1 and B2) is detected (Fig. 8c), suggesting two fcc-structured Co—Cu phase with different lattice constants and chemical compositions, which is in good agreement with the corresponding XRD spectra of this sample as presented in Fig. 5a. STEM-EDS analysis also confirms a multi-layered structure with strong compositional fluctuations of Co and Cu in this alloy (Fig. 8d,e). A major part of a multi-layered structure contains tens to hundreds of nanometer thick layers of the primary Co—Cu phase layers with 25–30 at.% Cu (Fig. 8f-g), which are attributed to the primary {111} peak (B1). The second part of multi-layered structure is arranged of <50 nm thin Co—Cu phase layers with a higher Cu composition. The concentrations of Cu in these layers are 10–15 at.% higher than in the surrounding Co—Cu layers as shown in Fig. 8h. These layers are representation of the secondary Co—Cu {111} peak (B2), confirming that the sample exhibits heterogeneous solid solution nanostructures (dual-phase alloy). In rest of this paper, the Cu-richer phase term refers to the secondary Co—Cu phase detected in dual-phase alloys.

Fig. 9a displays an inverse pole figure (IPF) map from the cross-section of heterogeneous/dual-phase alloy. In comparison to single-phase alloy, TEM-OIM analysis of dual-phase alloy shows an extensively higher fraction of tiny grains with sizes of below 20 nm as validated with a grain size distribution analysis in Fig. 9b. These grains are representative but not limited only to the microstructure of the thin Cu-richer phase layer as detected in Fig. 8f-h. The larger grains detected in this alloy are supposed to be the primary Co—Cu phase with the expected grain sizes in the range of 20–100 nm, which are identical to the grain sizes of sample with a homogeneous solid solution nanostructure. The XRD peak breadth analysis confirms that the grain size of primary Co—Cu phase in this sample is ~48 nm. The nanostructured grains in this samples also exhibits the predominantly {111} texture along the growth direction as shown in Fig. 9c.

3.3.3. *The Cu-rich surface layer*

TEM-BF images for single- and dual-phase alloys (Fig. 6a and Fig. 8a) also shows the presence of 100–200 nm thin layer of the coarser-grained structure at the top surface of the Co—Cu film with a significantly high concentration of Cu (Fig. 6g and Fig. 8g). This layer is supposed to be either the Cu-rich surface layer formed at the end stage of deposition process or the Cu-oxide layer formed due to oxidation process. Thus, additional STEM-EDS analysis for selected elements (i.e., Cu, Co, Pt, and O) was carried out at this particular area of interest as displayed in Fig. 10a-e. STEM-EDS analysis confirms that this surface layer exhibits an extremely high Cu concentration of beyond 90 at.%. On the other hand, EDS-line profile analysis (Fig. 10f) observes that the concentration of oxygen remains constant from the Cu-rich surface layer to the Co—Cu film. In addition, no significant peak intensity of oxygen is detected from the EDS spectra within this particular area of interest (see Fig. 10e,g). The concentration of oxygen is slightly higher in Pt-coating, where the different height surface profile of TEM-lamella surface have a contribution for this finding. The evidence confirm that there is a low chance for the significant presence of oxygen in the Cu-rich surface layer. Here, the oxygen detected from the measurement may be related to thin layer

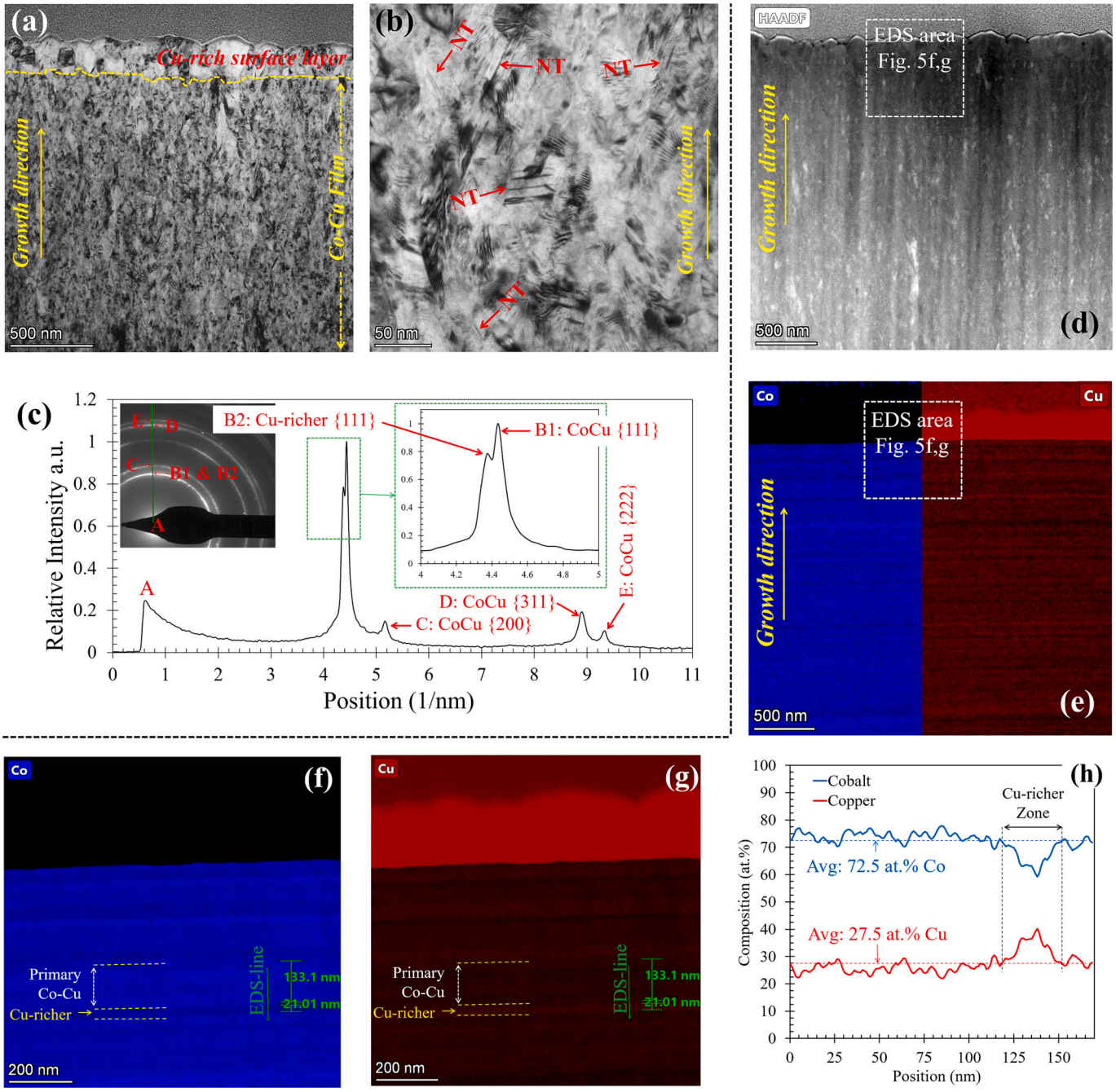

Fig. 8. TEM and STEM-EDS analysis from the cross-section of a heterogeneous/dual-phase Co—Cu alloy deposited with 0.5 g/L SDS (sample *S8*): (a-b) TEM-BF images and (c) the corresponding SAED pattern in Co—Cu film regime. (d) HAADF and (e) the corresponding EDS elemental maps of Co and Cu. (f-g) EDS elemental maps of (f) Co and (g) Cu at a selected area of interest and (g) the corresponding EDS line profiles along a green arrow marked within the elemental maps in (f) and (g).

of surface oxidation of TEM lamella sample, but its actual concentration is supposed to be lower as commonly observed from STEM-EDS analysis. Thus, the coarser-grained structure detected at the top surface of Co—Cu film is not Cu-oxide layer from oxidation process. Instead, this layer is supposed to be a Cu-rich surface layer developed at the end stage of deposition process. Interestingly, the peak intensity for the Cu-rich surface layer (see Fig. 6g) is surprisingly not visible from XRD line profile analysis. The peak intensity from this layer may be not significant for detection due to the low thickness ratio of this layer (100–200 nm) compared to a major part of Co—Cu film (20 μm). This evidence validates that the secondary/Cu-richer phases with an enhanced lattice constant observed by XRD and TEM analysis is related rather to the Cu-richer layers inside the Co—Cu coating and not to the Cu-rich surface layer.

The Cu-rich surface layers formation is proposed through the displacement reaction of deposited Co with Cu^{2+} ions during the retention time after deposition. The displacement reaction is possible during the off-time due to a large gap of the standard reduction potential (E^0_{Cu} = +0.34 V vs. SHE and E^0_{Co} = −0.28 V vs. SHE) as expressed by the following reaction.

$$Co_{(s)} + Cu^{2+}_{(aq)} \rightarrow Cu_{(s)} + Co^{2+}_{(aq)} \quad (2)$$

The displacement reaction and formation of tens of nanometer thick Cu-rich layer have been reported within the long off-time duration

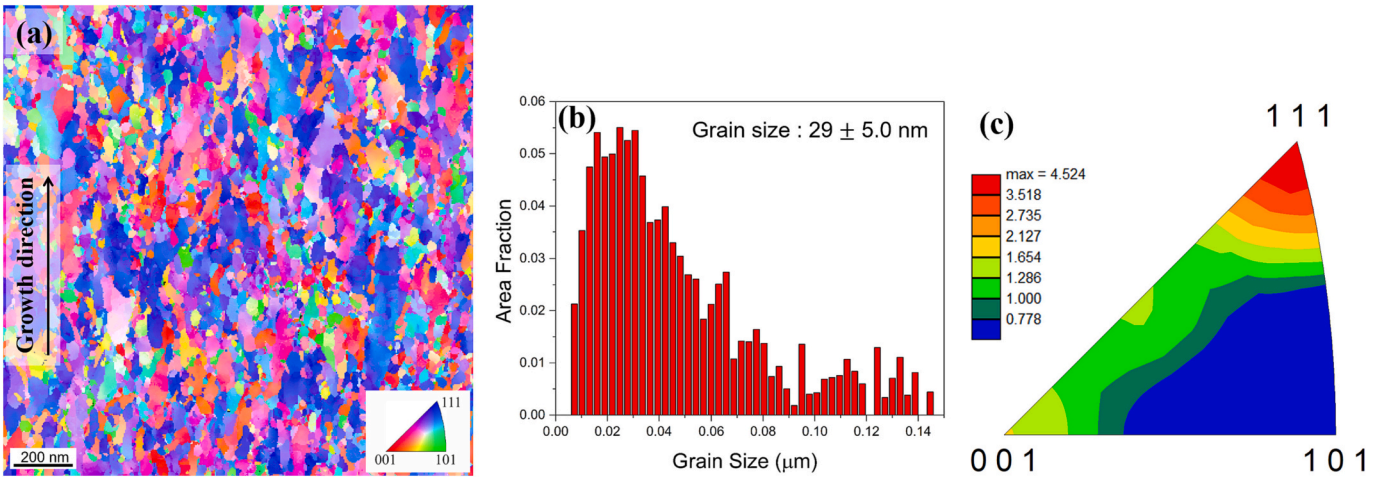

Fig. 9. TEM-OIM microstructure analysis along the cross-section of heterogeneous/dual-phase Co—Cu alloys: (a) Inverse pole figure (IPF) maps, (b) the corresponding grain size distribution, and (c) IPF texture analysis.

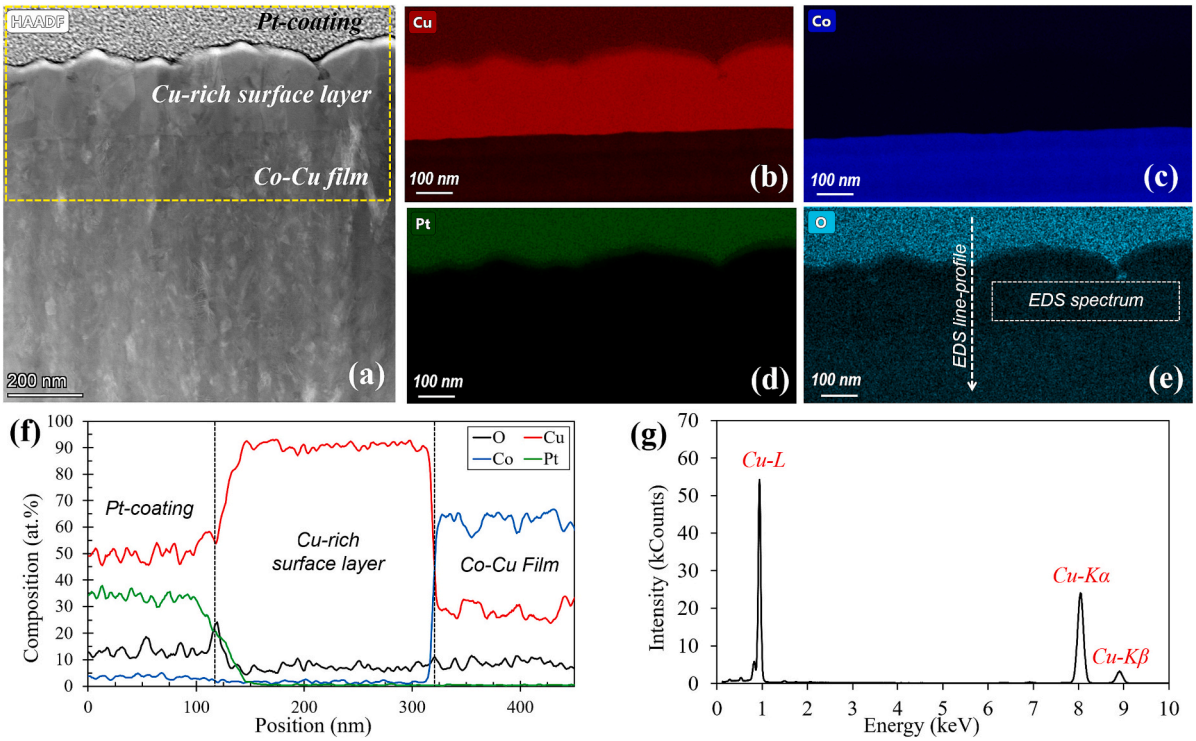

Fig. 10. STEM-EDS analysis from the cross-section of a heterogeneous/dual-phase Co—Cu alloy showing the presence of Cu-rich surface layer at the top surface of Co—Cu film: (a) HAADF and (b-e) the corresponding EDS elemental maps of Cu, Co, Pt, and O to investigate the possible formation of Cu-oxide layer at the top surface of Co—Cu film. (f) EDS line profiles along a white arrow marked in (e). (g) EDS spectra in the Cu-rich surface layer marked with a white rectangular shape in (e).

[13,14,42,43]. Interestingly, the thickness of Cu-rich surface layer for the dual-phase alloy with 0.5 g/L SDS (200–250 nm) is two times larger than measured for the single-phase alloy with 1.5 g/L SDS (~100 nm). Thus, SDS concentration should have a significant influences for the growth rate of this Cu-rich surface layer. In this case, SDS molecules may act as a barrier for displacement reaction, which limits the growth rate and the thickness of Cu-rich surface formed on the top surface of Co—Cu deposits.

3.3.4. *XRD vs. TEM-OIM grain size analysis*

For a single-phase alloy (sample *S10*), the grain size determined from XRD peak breadth analysis (~18 nm) is smaller than calculated from TEM-based OIM analysis (~40 nm) due to the different measurement and analysis techniques. In the following, some factors contributing to the difference is listed and discussed. *First*, XRD peak breadth analysis is very sensitive even to small misorientations angles within individual grains. In this particular case, the crystallite size observed from XRD analysis may be equivalent to the sub-grain size in microstructures where the individual grains are fragmented into sub-grains [36]. Thus, the crystallite size obtained from the XRD peak breadth analysis is also usually called as diffraction domain size. *Second*, XRD analysis investigates orders of magnitude larger volume of sample than TEM. Therefore, the difference between the crystallite size obtained by XRD and the grain size determined by microscopy analysis is not surprising.

Third, the quantity *D* in Eq. (1) is an apparent crystallite size and not the diameter of the diffraction domains. Namely, the Williamson-Hall analysis yields the volume-weighted mean column length where the columns are obtained by cutting the crystallites perpendicular to the reflecting lattice planes [36]. For instance, for spherical crystallites this volume-weighted mean column length is 33% smaller than the crystallite diameter. Therefore, the latter effect can yield a systematically lower value of the apparent crystallite size (*D*) obtained from Eq. (1) than the grain size determined from TEM. *Fourth*, XRD peak breadth approach performed in this particular analysis only evaluates the harmonic reflection pair of (111)–(222). On the other hand, TEM approach identifies all grains with various crystallographic orientations detected using OIM technique. Of course, there are also several other convolutional multiple whole profile (CMWP) models available [44], which gives grain size values nearly the same as TEM grain size. However, the texturing effect and number of peaks in the present study limits the use of such models for the analysis here.

3.4. Micropillar compression

The mechanical properties of NC Co—Cu alloys exhibiting a homogeneous/single-phase (sample *S10*) and a heterogeneous/dual-phase (sample *S8*) solid solution layered structures were investigated by quasistatic micro-pillar compression at room temperature. Representative engineering stress vs. engineering strain curves for single- and dual-phase alloys are presented in Fig. 11a. The yield strength analysis

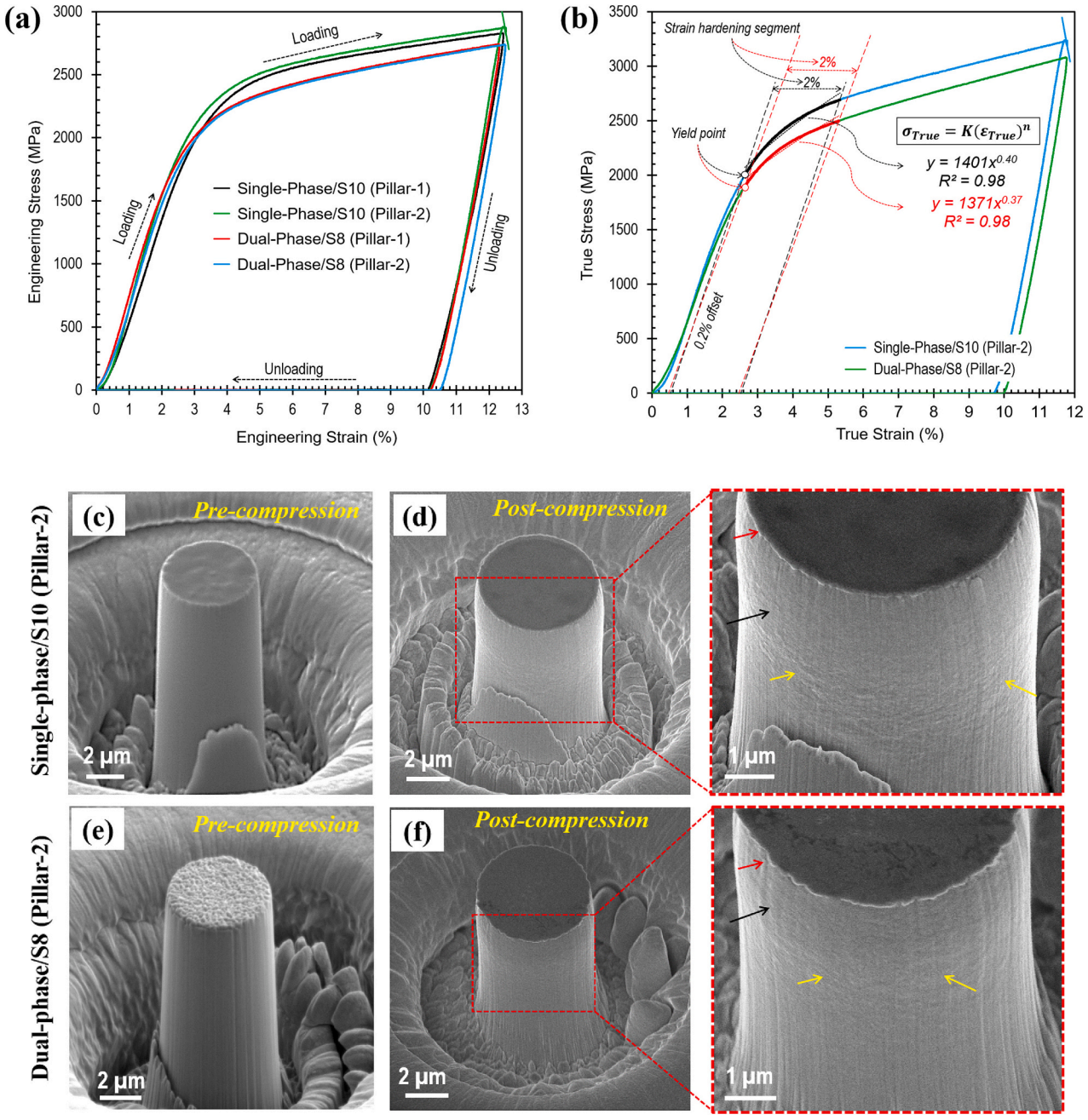

Fig. 11. (a) The representative engineering stress vs. strain curves for room temperature quasistatic micro-pillar compression of homogeneous/single-phase and heterogeneous/dual-phase NC Co—Cu alloys. (b) The representative true stress vs. strain curves for determination of strain hardening exponent. (c-f) Secondary electron (SE) micrographs of pre- and post-compression surface morphology of selected micro-pillars from (c-d) single- and (e-f) dual-phase alloys. It must be noted that pre- and post-compression images were taken at different tilt angles.

was performed by implementing 0.2% offset from the initial elastic segment. The mean yield strengths of single- and dual-phase NC Co—Cu alloys from five micro-pillars are 1.86 ± 0.04 GPa and 1.74 ± 0.04 GPa, respectively, which are the highest among the nanostructured Cu [45–52], Co [8,9,53,54], and Co—Cu alloys [3,5,17] investigated by other researchers.

Fig. 11a also shows that the apparent strain hardening is visible in the plastic regime, which is supposed to increase ductility and crack propagation resistance in NC alloys. Note that here we express it as apparent strain hardening as the strain hardening might be affected by such artifact as tapering and friction in pillar compression [55,56]. For validation, the corresponding true stress vs. stress curves were also plotted as presented in Fig. 11b. The strain hardening exponent (*n*-value) was determined by fitting the initial stage of plastic segment (i.e., 2% strain from the yield point) to the flow stress equation, $\sigma_{true} = K(\varepsilon_{true})^n$, as demonstrated in Fig. 11b. The analysis shows that the strain hardening exponents of these NC Co—Cu alloys micro-pillars are 0.40 ± 0.02 and 0.37 ± 0.01, respectively. The *n*-values are significantly higher than typical NC Co [8], Cu [57], and Co—Cu alloys [3] in the range of 0.20 to 0.23, indicating an improved ductility, formability, and crack propagation resistance for these NC Co—Cu alloys. In fact, the strain hardening of these alloys are comparable to that of NT Cu (n = 0.33–0.35) [51,58], which exhibit the highest tensile ductility up to 30% uniform elongation among nanostructured materials reported.

Post-mortem test surface morphology analysis was performed after compression by using SEM. For all micro-pillars fabricated from single- and dual-phase alloys, failure or even crack formation was not observed after the compression up to 12% of strain. The typical surface morphology characteristics of the micro-pillar after compression are depicted in Fig. 11d,f showing a bulging phenomenon predominantly at the upper part of the pillar, as indicated with a black arrow. A relatively strong surface roughness induced by the plastic deformation is observed as indicated by the green arrows. The red arrows in Fig. 11c,e show the fully compressed thin layer structures at the top surface of the micro-pillar. This extruded thin layer can be related to the Cu-rich surface layer with coarse-grained structure, as observed from TEM and STEM-EDS analysis. However, due to the negligible thickness compared to the entire pillar height, this Cu-rich surface layer should not significantly impact to the overall stress-strain curves.

4. Discussion

4.1. The roles of SDS on deposition and growth mechanism

The roles of SDS and the influence of its concentration on the deposition mechanisms and resulting deposits have been investigated through the various electrochemical and microstructure analysis. *First,* LSV and DC deposition analysis confirmed the role of SDS to promote the deposition of Co over Cu, which is further validated by the rising concentration of Co detected by EDS elemental analysis for both of DC and 5 ms on-time PED processed samples. Only a group of samples deposited at 2 ms on-time process exhibits a rather constant Co—Cu composition for varied SDS concentration, which is discussed further in Section 4.2. For 5 ms on-time process, the presence of SDS molecules in the vicinity of cathode surface may have a tendency to create ionic bonding with Co^{2+} over Cu^{2+} ions, which enhances the ionic mobility and deposition rate of Co. In contrast, Kim et al. [59] reported that SDS led to micellar effect, which stabilized Cu^{+} intermediate ions and decreased the ionic diffusion coefficient of Cu^{2+}. Thus, it was reported that SDS had no significant influence for the overall deposition rate of Cu.

Second, SDS molecules may also act as the barriers for displacement reactions of Co with Cu ions during the off-time, due to adsorption of this anionic surfactants on the cathode surface. This mechanism is validated by a much thinner Cu-rich surface layer formed in the present of a higher concentration of SDS as discussed in Section 3.3.3. This is the opposite SDS effect reported by Landolt et al. [14], where SDS stimulated the displacement reaction of Co with Cu ions during the off-time period. The different result may be influenced by some factors such as the different experimental setup (rotating disk vs. *static electrode*), pulsed current density (−400 A/m^2 vs. *-1000 A/m^2*), pulse-length (0.1–100 s vs. *0.02–0.5 s*), and electrolyte composition used for PED process.

Third, microstructure analysis through XRD and TEM observed that the formation of secondary solid solution or Cu-richer phase layers is strong dependence on SDS concentration. Here, the increasing concentration of SDS tends to stabilize the primary Co—Cu phase layer and to reduce the fraction/thickness of the Cu-richer phase layer. This could be the reason for the gradual decrease of XRD peak intensity of the Cu-richer phase as shown in Fig. 5a. For 5 ms on-time PED process, XRD analysis shows the adjacent peak position for the primary Co—Cu and the Cu-richer phase with 1.0 g/L SDS (Fig. 5a). Here, the phase separation and the gradient concentration are less strong compared to the samples deposited with the lower concentrations of SDS at 0.3 g/L and 0.5 g/L. The stabilization effect is more intense at the highest SDS concentration (1.5 g/L) used in this work, resulting in a homogeneous solid solution Co—Cu nanostructure. The potential profiles (Fig. 3) also revealed that the increase in SDS concentration leads to the minor shift of on-time potential to more positive value and off-time potential to more negative value, resulting in the narrower range of on-to-off-time potential (ΔE), which could be an indication for the altered chemical process. The stabilization effect was still reported for reduced pulsed length, despite the change in Co—Cu composition was not observed for 2 ms on-time PED process samples. However, the detailed mechanism of SDS influencing on the formation of homogeneous microstructure remained unknown. Thus, possible growth mechanisms for the primary and Cu-richer phase layer need to be discussed to obtain more in-depth understand of this stabilization effect.

Growth mechanisms for the primary and Cu-richer phase layers are evaluated in accordance with STEM-EDS elemental distribution analysis for heterogeneous/dual-phase alloy (Fig. 8d-h) deposited at t_{on} = 5 ms and t_{off} = 45 ms in the solution containing 0.5 g/L SDS. Here, it is assumed that the deposition of primary Co—Cu layer takes place during 5 ms on-time period. Simple calculations through the Faraday's second law of electrolysis were carried out to evaluate the theoretical deposited thickness of the primary Co—Cu phase layers as expressed by the following formula.

$$\text{Thickness} = \left(i_p.t_{on}.A_r\right)/(\rho.n.F) \quad (3)$$

A_r and ρ are the atomic mass relative and the mass density of $Co_{70}Cu_{30}$. The other parameters are the number of involved electrons (n = *2*) and the Faraday constant (F = 96,485 A.s.mol^{-1}). For a single pulse cycle with t_{on} = 5 ms and i_p = 1000 A/m^2, the theoretical deposited thickness of Co—Cu layer is ~180 pm, which corresponds to the atomic radius of Co (200 pm) or Cu (128 pm), suggesting that a Co—Cu monolayer is deposited for a single pulse cycle. On the other hand, STEM-EDS analysis (Fig. 8d-h) confirms that the apparent thickness of the primary Co—Cu layers is ranging in tens to hundreds of nanometers, suggesting that multiple pulse cycles are needed to deposit the primary Co—Cu phase layer. Thus, the formation of Cu-richer phase layer does not occur within this pulse cycle. In this particular case, it is suggested that the Cu-richer layer is not developed through the displacement reaction during the off-time period, which is validated by some evidences and given calculation. *First*, the potential profile during PED process observed that the maximum off-time potential is −0.40 V vs. Ag/AgCl (see Fig. 3c), which is out of the range of dissolution potential for Co started from +0.135 V vs. Ag/AgCl to more positive potentials [60]. Thus, there is small chance for the displacement reaction occurs at the recorded off-time potential. *Second*, the theoretical calculation also shows that the required current density for the formation of ~21 nm thin Cu-richer layer through displacement reaction is 1900 A/m^2 (detailed calculation is available in Supplementary Materials C), which is much higher than the off-time current density recorded in the range of 1–2 A/

m^2 (see Fig. 2a). The required current density is also much higher than the limiting current density of Cu obtained from the LSV curves in the range of 20–40 A/m^2 (see Fig. 1a), which is supposed to be the maximum rate of displacement reaction as reported in the literature [42,61]. The evidences and given calculation show that the Cu-richer phase layer is mainly growing by another mechanism and not in a single pulse cycle.

Here, the growth mechanism for the secondary phase layer is proposed through the deposition of Cu-richer layer due to periodical concentration fluctuation of Co^{2+} ions in the vicinity of electrode surface occurs for multiple pulse cycles. Here, it is assumed that the deposition rate of Cu remain constant at varied SDS concentration as proposed by Kim et al. [59] and validated by LSV analysis in Fig. 1a. LSV and EDS compositional analysis suggest that SDS molecules tend to enhance the ionic mobility of Co^{2+} ion, which brings this ion closer to the cathode surface over Cu^{2+} ion. Thus, a fairly stable concentration of Co^{2+} ion can be maintained at the vicinity of cathode surface for multiple pulse cycles in the presence of a high concentration of 1.5 g/L SDS, resulting in a homogeneous structure Co—Cu deposit. This is also validated by the minor shift of the on-time potential to more positive value with increasing SDS concentration (see Fig. 3b), indicating the lower energy and more favorable condition for deposition of Co. For the lower SDS concentrations (e.g., 0.5 g/L), the ionic mobility of Co^{2+} ions may decrease, which influences for the periodical concentration fluctuation of Co^{2+} ion at the vicinity of cathode surface for deposition. Thus, NC alloy deposited at the lower SDS concentration (e.g., 0.5 g/L) may exhibit a compositional modulation of Co—Cu and heterogeneous solid solution microstructure differing in 10–15 at.% Cu as observed in dual-phase alloy. Further decrease of SDS concentration may lead to more frequent concentration fluctuation of Co^{2+} ion, resulting in more frequent compositional modulation and increased fraction of Cu-richer phase layer.

4.2. The influence of pulse-length on deposition mechanism

The potential profiles from pulse galvanostatic analysis in Section 3.1 show the significantly broader range of deposition potentials (ΔE in Fig. 1c) with extended pulse length, which could be the indication for increasing thickness of the pulsating diffusion layer. Moreover, the samples deposited at varied pulse-length also exhibit the altered chemical compositions and microstructures. Fig. 12a shows a schematic illustration showing the concentration diffusion layer during PED process after multiple pulse cycles (i.e., quasi-steady-state) for different pulsed length at the same duty cycle. For PED process, the Nernst diffusion layer consists of the pulsating (δ_p) and the stationary (δ_s) Nernst diffusion layer. The thickness ratio of the pulsating diffusion layer is $\delta_{p,2ms}$: $\delta_{p,5ms}$:$\delta_{p,50ms}$ = 1: $\sqrt{2.5}$: 5, according to Ibl [38,62]. The schematic illustration (Fig. 12a) shows that for the same electrolyte composition in the bulk electrolyte, the concentrations of metallic cations and organic additives (SDS) at the vicinity of electrode surface are higher for the shorter pulse length. Thus, the increase in the Co composition (see Table 1) with the shorter pulse length may be influenced by the increase concentrations of Co^{2+} and SDS at the vicinity of electrode surface. Here, SDS acts particularly to promote the deposition of Co over Cu as discussed in Section 4.1. Moreover, the higher SDS concentration also supports to stabilize the primary solid solution Co—Cu structure, which is validated by the significant decrease in the fraction of the Cu-richer phase layer as observed from their corresponding XRD spectra (Fig. 12b). For 2 ms on-time PED process, the diffusion layer may be not thick enough to introduce the large gradient concentration of Co^{2+} ions ($C_M^b - C_M^e$), resulting in a rather constant Co—Cu composition for varied SDS concentration. The constant concentration can be influenced also by too short on-time period for SDS molecules to be adsorbed in the vicinity of cathode surface and to create ionic bonding with Co^{2+} ions. Interestingly, in this group of samples, the adsorbed SDS molecules still play a vital role in stabilizing the primary solid solution Co—Cu structure as observed from their XRD spectra (see Fig. 5b).

4.3. Strengthening mechanism in single- and dual-phase alloy

The micro-pillar compression of single- and dual-phase of solid solution NC Co—Cu alloys revealed that these PED-processed materials exhibited the highest yield strength among the nanostructured Co, Cu, and Co—Cu alloys investigated through the tensile and compression experiments as depicted in Fig. 13a,b. The referred data points were all tested at a quasi-static condition (in the range of 10^{-3} s^{-1} to 10^{-4} s^{-1}) to minimize the discrepancy induced by testing strain rates. With sufficient data points, the strength of NC/NT Cu with different grain size/twin spacing [45–52] can be fit by a Hall-Petch relationship [63]. With

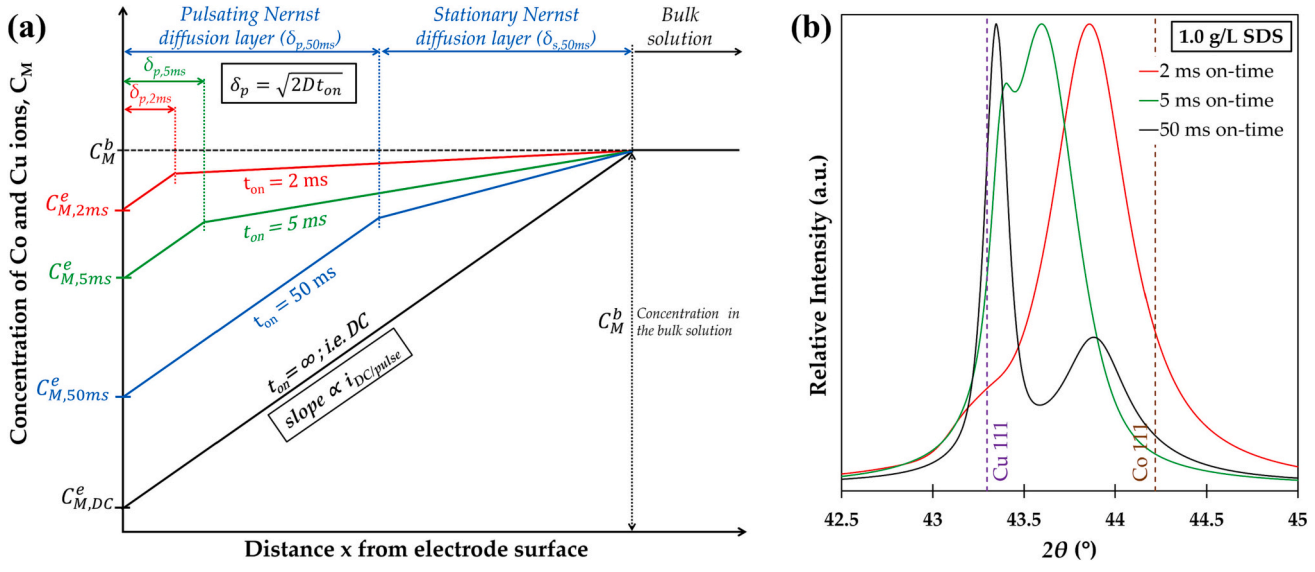

Fig. 12. (a) Schematic illustration of the pulsating and stationary Nernst diffusion layer during the quasi-steady-state PED process for different pulsed length with the same duty cycle. The single Nernst diffusion layer is also modeled for DC process. The slope or gradient concentration in the pulsating diffusion layer is proportional to the pulsed current density ($i_{pulse/DC}$) according to the Fick's law of diffusion: $i_{pulse/DC} = -zFD\left[\left(C_M^b - C_M^e\right)/\delta_p\right]$. (b) Detailed XRD spectra for a group of samples deposited at varied pulsed length with the same 1.0 g/L SDS concentration.

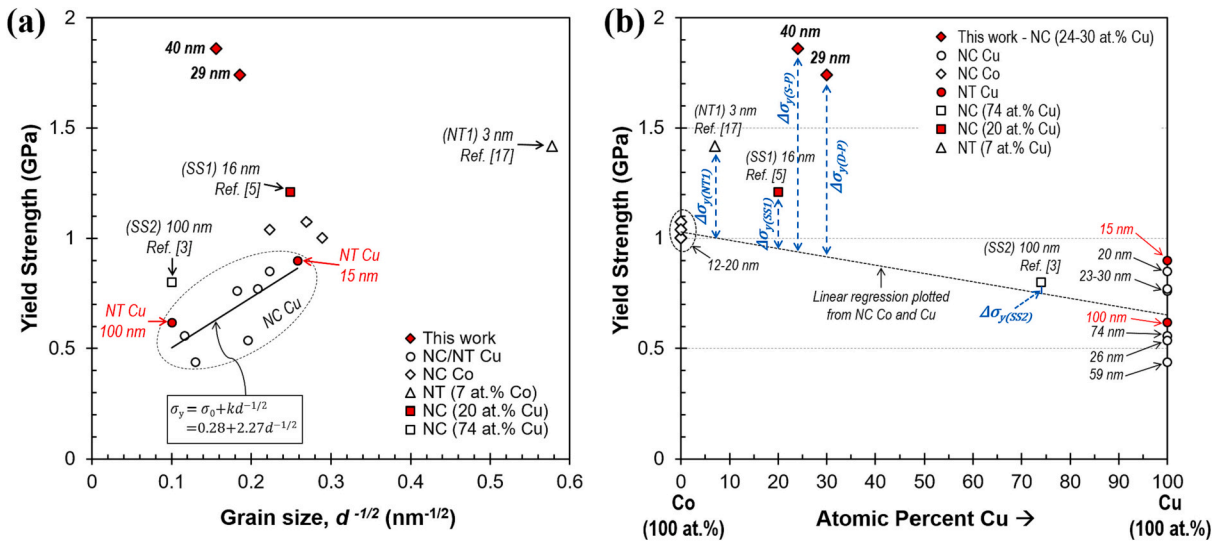

Fig. 13. The yield strength of nanostructured Co, Cu, and Co—Cu alloys as a function of (a) the grain size or twin spacing in the Hall-Petch plot ($d^{-1/2}$) and (b) the atomic percent of Cu. The regression in (b) is representative of the theoretical yield strength of NC Co_XCu_Y ($\sigma_{y,Co_XCu_Y} = \sigma_{y,Co}X\% + \sigma_{y,Cu}Y\%$) with no strengthening effect is expected from this mixture. The parameter $\Delta\sigma_y$ corresponds to the strengthening effect in the particular Co—Cu compositions. *NT*: Nano-twin hardening, *SS*: solid solution strengthening, *S-P/D-P*: hardening in single- and dual-phase alloys. Data were collected from various literature: NC Cu [45–50], NT Cu [51,52], NC Co [8,9,53,54], NC Co—Cu [3,5], NT Co—Cu [17].

similar grain size, the yield strength of NC Co samples with hcp structure (~1.0 GPa [8,9,53,54]) is superior to all NC/NT. After mixed with Cu, the Co—Cu alloys is further strengthened (Fig. 13b). This suggest that the high strength of our NC Co—Cu alloys are not only contributed by the fine grain size/twin spacing, but also solid solution hardening. Note that with a comparable Cu content, our NC alloys are superior than another NC Co—Cu alloys with a solid solution structure (*SS1* [5]), which has even smaller grain size. This can results from the anisotropy of compression and tension as well as abundant nano twins inside our materials as observed from TEM analysis. To summarize, the evidences suggest that the prominent strengthening effect in our NC Co—Cu alloys is contributed by a combined solid solution strengthening and hardening through NT.

The micro-pillar compression of a single-phase alloy shows a slightly higher strength compared to a dual-phase one. Based on microstructural analysis (Section 3.2), the single-phase alloy exhibits a homogeneous NC Co—Cu solid solution structure with 24 at.% Cu, as illustrated in Fig. 14a. In contrast, the dual-phase alloy with 32 at.% Cu is a multi-layered like nanostructure contains the primary solid solution Co—Cu layers (25 at.% Cu) with the thickness of tens of nanometers and the Cu-richer phase layers (40 at.% Cu) with the thickness of below 30 nm, as illustrated in Fig. 14b. *First,* the higher Co content in the single-phase alloy can lead to the increased strength in NC Co—Cu alloys. This is also validated by a higher yield strength of the Co-rich NC Co—Cu alloys [5] than the Cu-rich one [3] differing for ~400 MPa with 54 at.% gap in Co composition. *Second,* the grain size of the primary Co—Cu phase in the dual-phase alloy is more than twice larger than for the single-phase alloy as observed from XRD grain size analysis (~48 nm versus ~18 nm as determined from the integral breadth for (111)–(222) harmonic reflections, see Fig. 5c), where the increasing SDS concentration drives for the grain refinement. Thus, the grain size reduction strengthening could be one of the reason for the higher strength in the single-phase alloy. The Hall-Petch relationship [63] suggests that the strength increase in polycrystalline materials is proportional to the inverse square root of the grain size. Putting the grain size of the primary Co—Cu phase into the Hall-Petch relationship, the theoretical strength ratio in a single- to a

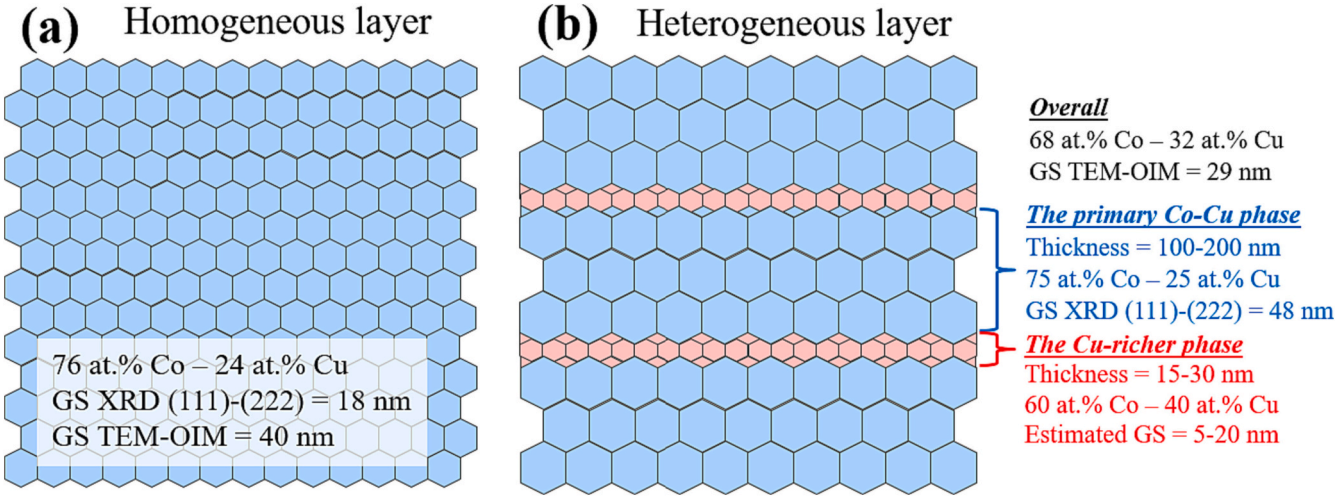

Fig. 14. The schematic illustrations of microstructure configuration for (a) a homogeneous/single-phase and (b) a heterogeneous/dual-phase layered nanostructures. GS: grain size.

dual-phase alloys is 1.63 obtained from $\frac{\sigma_{single}}{\sigma_{dual}} \cong \left(\frac{18\ nm}{48\ nm}\right)^{-\frac{1}{2}}$, which is higher than their actual yield strength ratio of 1.06 calculated from $\frac{\sigma_{actual\ single}}{\sigma_{actual\ dual}} = \frac{1.86\ GPa}{1.74\ GPa}$. It should be noted that the strength formula in Hall-Petch contains not only the grain size term, but also a friction stress or a yield strength of single crystals or coarse grains of these materials. However, the value of this parameter is supposed to be much lower compared to the yield strength of NC materials and it can be assumed negligible. The given calculations reveal that the actual yield strength of dual-phase alloy is higher than predicted from the Hall-Petch relationship. Thus, there should be additional strengthening mechanism in dual-phase alloy. The Cu-richer phase structure is believed to provide a foremost contribution to the increase of yield strength in dual-phase alloy. TEM-based OIM analysis (Fig. 7b,d,f) confirms that this Cu-richer phase layer contains very fine nanostructure grains with sizes of 5–20 nm as illustrated in Fig. 14b, which is much finer than the primary Co—Cu phase. This fine-grained structure is supposed to exhibit a higher yield strength than the primary Co—Cu phase layer, which contributes to the strengthening effect in the dual-phase alloy. *Last*, the strengthening mechanism in these NC alloys is also contributed by other factors, such as the different density and characteristic of nano-twin, which is clearly visible from TEM observation (see Fig. 6b,c and Fig. 8b). However, a more comprehensive understand of such nano-twin structure needs further investigation, which is not the scope of this paper.

5. Conclusion

PED of NC Co—Cu alloys with a homogeneous/single-phase and a heterogeneous/dual-phase of solid solution layered structures has been successfully performed at varied SDS concentrations and pulse lengths. The increasing concentration of SDS had a major contribution to multiple aspects related to the chemical composition and microstructure of NC Co—Cu films. These are: *(i)* promote the deposition of Co over Cu, *(ii)* stabilize the growth of a homogenous solid solution Co—Cu structure, *(iii)* grain size reduction, and *(iv)* improve surface morphology. Here, the gradual phase separation and formation of a multilayered structure consisting of the primary and secondary (Cu-richer) solid solution Co—Cu layers were observed with decreasing the concentration of SDS.

Micro-pillar compression for selected single- and dual-phase NC Co—Cu alloys revealed the highest yield strength among nanostructured Co, Cu, and Co—Cu alloys. The strengthening mechanisms were contributed by grain size reduction, solid solution strengthening, and the hardening of nano-twins. These alloys showed also a significant strain hardening, which may lead to increased ductility and crack propagation resistance.

TAED of NC Co—Cu have been succeeded using the Co—Cu electrolyte used in this study for producing micro-pillars and micro-gears. The micro-sized structures also showed a superior surface quality. Further improvement is needed for reducing of mainly the internal stress of deposited structure.

CRediT authorship contribution statement

Killang Pratama: Writing – original draft, Visualization, Methodology, Investigation, Formal analysis, Data curation, Conceptualization. **Chunhua Tian:** Writing – review & editing, Investigation, Data curation. **Amit Sharma:** Writing – review & editing, Software, Investigation, Formal analysis, Data curation. **Maria Watroba:** Writing – review & editing, Visualization, Investigation, Formal analysis, Data curation. **Jenő Gubicza:** Writing – review & editing, Validation, Supervision, Formal analysis. **Bonita Dilasari:** Writing – review & editing, Validation, Supervision, Formal analysis. **Jakob Schwiedrzik:** Writing – review & editing, Supervision, Resources, Funding acquisition. **Johann Michler:** Writing – review & editing, Supervision, Resources, Funding acquisition.

Declaration of competing interest

The authors declare that they have no known competing financial interests or personal relationships that could have appeared to influence the work reported in this paper.

Data availability

Data will be made available on request.

Acknowledgment

This research did not receive any specific grant from funding agencies in the public, commercial, or not-for-profit sectors.

Appendix A. Supplementary data

Supplementary data to this article can be found online at https://doi.org/10.1016/j.surfcoat.2024.130613.

References

[1] A. Bachmaier, C. Motz, Mater. Sci. Eng. A. 624 (2015) 41–51, https://doi.org/10.1016/j.msea.2014.11.062.
[2] A. Bachmaier, M. Pfaff, M. Stolpe, H. Aboulfadl, C. Motz, Acta Mater. 96 (2015) 269–283, https://doi.org/10.1016/j.actamat.2015.05.053.
[3] A. Bachmaier, G. Rathmayr, J. Schmauch, N. Schell, A. Stark, N. Jonge, R. Pippan, J. Mater. Res. 34 (2018) 58–68, https://doi.org/10.1557/jmr.2018.185.
[4] K. Pratama, J. Barrirero, F. Mücklich, C. Motz, Materials 13 (2020) 2616, https://doi.org/10.3390/ma13112616.
[5] K. Pratama, C. Motz, Molecules 25 (2020) 5914, https://doi.org/10.3390/molecules25215194.
[6] G. Hibbard, K. Aust, G. Palumbo, U. Erb, Scr. Mater. 44 (2001) 513–518, https://doi.org/10.1016/S1359-6462(00)00628-X.
[7] G. Hibbard, K. Aust, U. Erb, Acta Mater. 54 (2006) 2501–2510, https://doi.org/10.1016/j.actamat.2006.01.028.
[8] A. Karimpoor, U. Erb, K. Aust, G. Palumbo, Scr. Mater. 49 (2003) 651–656, https://doi.org/10.1016/S1359-6462(03)00397-X.
[9] A. Karimpoor, U. Erb, Phys. Status Solidi 203 (2006) 1265–1270, https://doi.org/10.1002/pssa.200566157.
[10] L. Lu, N. Tao, L. Wang, B. Ding, K. Lu, J. App. Phys. 89 (2001) 6408–6414, https://doi.org/10.1063/1.1367401.
[11] L. Lu, L. Wang, B. Ding, K. Lu, J. Mater. Res. 15 (2000) 270–273, https://doi.org/10.1557/JMR.2000.0043.
[12] A. Bachmaier, M. Stolpe, T. Müller, C. Motz, IOP Conf. Ser.: Mater. Sci. Eng. 89 (2015) 1–9, https://doi.org/10.1088/1757-899X/89/1/012017.
[13] P. Bradley, D. Landolt, Electrochim. Acta 45 (1999) 1077–1087, https://doi.org/10.1016/S0013-4686(99)00301-1.
[14] J. Kelly, P. Bradley, D. Landolt, J. Electrochem. Soc. 147 (2000) 2975–2980, https://doi.org/10.1149/1.1393634.
[15] D. Landolt, A. Marlot, Surf. Coat. Tech. 169-170 (2003) 8–13, https://doi.org/10.1016/S0257-8972(03)00042-2.
[16] S. Ghosh, T. Bera, C. Saxena, S. Bhattacharya, G. Dey, J. Alloys Compd. 475 (2009) 676–682, https://doi.org/10.1016/j.jallcom.2008.07.137.
[17] Y. Nakamoto, M. Yuasa, Y. Chen, H. Kusuda, M. Mabuchi, Scr. Mater. 58 (2008) 731–734, https://doi.org/10.1016/j.scriptamat.2007.12.013.
[18] M. Yuasa, H. Nakano, Y. Nakamoto, M. Hakamada, M. Mabuchi, Mater. Trans. 50 (2009) 419–422, https://doi.org/10.2320/matertrans.MRP2008220.
[19] M. Yuasa, H. Nakano, K. Kajikawa, T. Nakazawa, M. Mabuchi, Mater. Res. Soc. Symp. Proc. 1224 (2009) 1032, https://doi.org/10.1557/PROC-1224-FF10-32.
[20] T. Müller, Pulsed Electrodeposition of Nanocrystalline Cobalt and Copper-Cobalt Alloys, Master Thesis of Saarland University, 2014.
[21] Berkowitz, J. Mitchell, J. Carey, A. Young, S. Zhang, F. Spada, F. Parker, A. Hutten, G. Thomas, Phys. Rev. Lett. 68 (1992), 3745–3748, doi:https://doi.org/10.1103/PhysRevLett.68.3745)https://doi.org/10.1103/PhysRevLett.68.3745).
[22] Y. Ueda, M. Ito, Magnetoresistance in co-cu alloy films formed by electrodeposition method, Jpn. J. Appl. Phys. 33 (1994) 1403–1405, https://doi.org/10.1143/JJAP.33.L1403.
[23] I. Rose, C. Whittington, Nickel Plating Handbook, Nickel Institute, Brussels, Belgium, 2014.
[24] J.R. Lopez, L. Flores, P.F. Mendez, J.J. Perez Bueno, G. Trejo, Y. Meas, J. Electrochem. Soc. 168 (2021) 062516, https://doi.org/10.1149/1945-7111/ac0c34.
[25] U.S. Mohanty, B.C. Tripathy, S.C. Das, P. Singh, V.N. Misra, Hydrometallurgy 100 (2009) 60–64, https://doi.org/10.1016/j.hydromet.2009.10.003.
[26] F. Jia, K.X. Wei, W. Wie, Q.B. Du, I.V. Alexandrov, J. Hu, J. Mater. Eng. Perform. 29 (2020) 897–904, https://doi.org/10.1007/s11665-020-04674-4.

[27] P. Schürch, R. Ramachandramoorthy, L. Pethö, J. Michler, L. Philippe, Appl. Mater. Today 18 (2020) 100472, https://doi.org/10.1016/j.apmt.2019.100472.
[28] P. Schürch, L. Pethö, J. Schwiedrzik, J. Michler, L. Philippe, Adv. Mater. Technol. 3 (2018) 1800274, https://doi.org/10.1002/admt.201800274.
[29] C.V. Manzano, P. Schürch, L. Pethö, G. Bürki, J. Michler, L. Philippe, J. Electrochem. Soc. 166 (2019) E310–E316, https://doi.org/10.1149/2.0961910jes.
[30] J. Schiwiedrzik, R. Ramachandramoorthy, T.E.J. Edwards, P. Schürch, D. Casari, M.J. Duarte, G. Mohanty, G. Dehm, X. Maeder, L. Philippe, J.M. Breguet, J. Michler, Mater. Des. 220 (2022) 110836, https://doi.org/10.1016/j.matdes.2022.110836.
[31] A. Hara, Z. Swiatek, P. Ozga, J. Alloys Compd. 827 (2020) 154195, https://doi.org/10.1016/j.jallcom.2020.154195.
[32] E. Michailova, M. Peykova, D. Stoychev, A. Milchev, J. Electroanal. Chem. 366 (1994) 195–202, https://doi.org/10.1016/0022-0728(93)03228-H.
[33] F. Su, C. Liu, Q. Zuo, P. Huang, M. Miao, Mater. Chem. Phys. 139 (2013) 663–673, https://doi.org/10.1016/j.matchemphys.2013.02.014.
[34] V. Otieno-Alego, G.A. Hope, H.J. Flitt, G.A. Cash, D.P. Schweinsberg, Corr. Sci. 33 (1992) 1719–1734, https://doi.org/10.1016/0010-938X(92)90004-M.
[35] M. Wojdyr, J. Appl. Cryst. 43 (2010) 1126–1128, https://doi.org/10.1107/S0021889810030499.
[36] J. Gubicza, X-Ray Line Profile Analysis in Materials Science, IGI-Global, Hershey, PA, USA, 2014. ISBN: 978-1-4666-5852-3.
[37] J. Portillo, E.F. Rauch, S. Nicolopoulos, M. Gemmi, D. Bultreys, Mater. Sci. Forum 664 (2010) 1–7, https://doi.org/10.4028/www.scientific.net/MSF.644.1.
[38] N. Ibl, Surf. Techno. 10 (1980) 81–104, https://doi.org/10.1016/0376-4583(80)90056-4.
[39] R. Winand, Hydrometallurgy 29 (1992) 67–598, https://doi.org/10.1016/0304-386X(92)90033-V.
[40] G.K. Williamson, W.H. Hall, Acta Metall. 1 (1953) 22–31, https://doi.org/10.1016/0001-6160(53)90006-6.
[41] M. El-Tahawy, L. Peter, L.F. Kiss, J. Gubicza, Z.S. Czigany, G. Molnar, I. Bakony, J. Magn. Magn. Mater. 560 (2022) 169660, https://doi.org/10.1016/j.jmmm.2022.169660.
[42] S. Roy, M. Matlosz, D. Landolt, J. Electrochem. Soc. 141 (1994) 1509, https://doi.org/10.1149/1.2054954.
[43] S. Roy, D. Landolt, J. Electrochem. Soc. 142 (1995) 3021, https://doi.org/10.1149/1.2048679.
[44] A. Sharma, S. Chhangani, R. Madhavan, S. Suwas, J. Magn. Magn. Mater. 434 (2017) 68–77, https://doi.org/10.1016/j.jmmm.2016.12.146.
[45] Y.M. Wang, K. Wang, D. Pan, K. Lu, K.J. Hemker, E. Ma, Scr. Mater. 48 (2003) 1581–1586, https://doi.org/10.1016/S1359-6462(03)00159-3.
[46] R.K. Guduru, K.A. Darling, R.O. Scattergood, C.C. Koch, K.L. Murty, J. Mater. Sci. 42 (2007) 5581–5588, https://doi.org/10.1007/s10853-006-1095-3.
[47] K.M. Youssef, R.O. Scattergood, K.L. Murty, C.C. Koch, Appl. Phys. Lett. 85 (2004) 929–931, https://doi.org/10.1063/1.1779342.
[48] P.G. Sanders, C.J. Youngdahl, J.R. Weertman, Mater. Sci. Eng. A. 234–236 (1997) 77–82, https://doi.org/10.1016/S0921-5093(97)00185-8.
[49] S. Bansal, A.M. Saxena, T. Hatwig, R.R. Tummala, J. Metastable Nanocryst. Mater. 23 (2005) 183–186, https://doi.org/10.4028/www.scientific.net/JMNM.23.183.
[50] M. Legros, B.R. Elliot, M.N. Rittner, J.R. Weertman, K.J. Hemker, Phil. Mag. A 80 (2000) 1017–1026, https://doi.org/10.1080/01418610008212096.
[51] Y.F. Shen, L. Lu, Q.H. Lu, Z.H. Jin, K. Lu, Scr. Mater. 52 (2005) 989–994, https://doi.org/10.1016/j.scriptamat.2005.01.033.
[52] M. Mieszala, G. Guillonneau, M. Hasegawa, R. Raghavan, J.M. Wheeler, S. Mischler, J. Michler, L. Philippe, Nanoscale 8 (2016) 15999–16004, https://doi.org/10.1039/C6NR05116B.
[53] Y.M. Wang, R.T. Ott, T. van Buuren, T.M. Wiley, M.M. Biener, A.V. Hamza, Physi. Rev. B 85 (2012), 014101, doi: https://doi.org/10.1103/PhysRevB.85.014101.
[54] X. Luo, C.Y. Chen, T.F.M. Chang, M. Sone, Q. Zhang, J. Zhang, J. Electrochem. Soc. 168 (2021) 102502, https://doi.org/10.1149/1945-7111/ac2be9.
[55] G. Dehm, B.N. Jaya, R. Rghavan, C. Kirchlechner, Acta Mater. 142 (2018) 248–282, https://doi.org/10.1016/j.actamat.2017.06.019.
[56] M. Schamel, J.M. Wheeler, C. Niederberger, J. Michler, A. Sologubenko, R. Spolenak, Philos. Mag. 96 (32–34) (2016) 3479–3501, https://doi.org/10.1080/14786435.2016.1235290.
[57] L. Lu, L.B. Wang, B.Z. Ding, K. Lu, J. Mater. Res. 15 (2000) 270–273, https://doi.org/10.1557/JMR.2000.0043.
[58] L. Lu, X. Chen, X. Huang, K. Lu, Science 323 (2009) 607–610, https://doi.org/10.1126/science.1167641.
[59] I.U. Kim, Y.R. Gwon, Y.M. Shin, S.K. Cho, Trans. IMF 100 (2022) 152–158, https://doi.org/10.1080/00202967.2021.2020440.
[60] S.M.S.I. Dulal, E.A. Charles, S. Roy, J. Appl. Electrochem. 34 (2004) 151–158, https://doi.org/10.1023/B:JACH.0000009945.92160.25.
[61] P. Fricoteaux, J. Douglade, Surf. Coat. Technol. 184 (2004) 63–68, https://doi.org/10.1016/j.surfcoat.2003.10.002.
[62] N. Ibl, J.Cl. Puippe, H. Angerer, Surf. Technol. 6 (1978) 287–300, https://doi.org/10.1016/0376-4583(78)90044-4.
[63] E. Hall, Proc. Phys. Soc. B 64 (1951) 747, https://doi.org/10.1088/0370-1301/64/9/303.